SELECTION FIELD INDUCED ARTIFACTS IN MAGNETIC PARTICLE IMAGING AND A NOVEL FRAMEWORK FOR NANOPARTICLE CHARACTERIZATION

A THESIS SUBMITTED TO

THE GRADUATE SCHOOL OF ENGINEERING AND SCIENCE

OF BILKENT UNIVERSITY

IN PARTIAL FULFILLMENT OF THE REQUIREMENTS FOR

THE DEGREE OF

MASTER OF SCIENCE

IN

ELECTRICAL AND ELECTRONICS ENGINEERING

By

Ecrin Yağız

October 2020

Selection Field Induced Artifacts in Magnetic Particle Imaging And a Novel Framework for Nanoparticle Characterization
By Ecrin Yağız
October 2020

We certify that we have read this thesis and that in our opinion it is fully adequate, in scope and in quality, as a thesis for the degree of Master of Science.

Emine Ülkü Sarıtaş Çukur(Advisor)

Can Barış Top(Co-Advisor)

Ergin Atalar

Yeşim Serinağaoğlu Doğrusöz

Approved for the Graduate School of Engineering and Science:

Ezhan Karaşan
Director of the Graduate School

ABSTRACT

SELECTION FIELD INDUCED ARTIFACTS IN MAGNETIC PARTICLE IMAGING AND A NOVEL FRAMEWORK FOR NANOPARTICLE CHARACTERIZATION

Ecrin Yağız
M.S. in Electrical and Electronics Engineering
Advisor: Emine Ülkü Sarıtaş Çukur
Co-Advisor: Can Barış Top
October 2020

Magnetic particle imaging (MPI) is a recent imaging modality that uses non-linear magnetization curves of the superparamagnetic iron oxides. One of the main assumptions in MPI is that the selection field changes linearly with respect to the position, whereas in practice it deviates from its ideal linearity in regions away from the center of the scanner. The first part of this thesis demonstrates that unaccounted non-linearity of the selection field causes warping in the image reconstructed with a standard x-space approach. Unwarping algorithms can be applied to effectively address this issue, once the displacement map acting on the reconstructed image is determined. The unwarped image accurately represents the locations of nanoparticles, albeit with a resolution loss in regions away from the center of the scanner due to the degradation in selection field gradients. In MPI, the relaxation behavior of the nanoparticles can also be used to infer about nanoparticle characteristics or the local environment properties, such as viscosity and temperature. As the nanoparticle signal also changes with drive field (DF) parameters, one potential problem for quantitative mapping applications is the optimization of these parameters. In the second part of this thesis, a novel accelerated framework is proposed for characterizing the unique response of a nanoparticle under different environmental settings. The proposed technique, called "Magnetic Particle Fingerprinting" (MPF), rapidly sweeps a wide range of DF parameters, mapping the unique relaxation fingerprint of a sample. This technique can enable simultaneous mapping of several parameters (e.g., viscosity, temperature, nanoparticle type, etc.) with significantly reduced scan time.

Keywords: magnetic particle imaging, magnetic nanoparticles, artifacts, nanoparticle characterization, mapping.

ÖZET

MANYETİK PARÇACIK GÖRÜNTÜLEMEDE SEÇME ALANI KAYNAKLI ARTEFAKTLAR VE ÖZGÜN BİR NANOPARÇACIK KARAKTERİZASYON YÖNTEMİ

Ecrin Yağız
Elektrik ve Elektronik Mühendisliği, Yüksek Lisans
Tez Danışmanı: Emine Ülkü Sarıtaş Çukur
İkinci Tez Danışmanı: Can Barış Top
Ekim 2020

Manyetik Parçacık Görüntüleme (MPG) süperparamanyetik demir oksitlerin doğrusal olmayan manyetiklenme eğrilerini kullanan yeni bir görüntüleme yöntemidir. MPG'de sıkça yapılan varsayımlardan biri seçme alanının konuma göre doğrusal değişmesidir, ancak pratikte tarayıcının merkezinden uzaklaştıkça ideal doğrusallıktan da uzaklaşılmaktadır. Bu tezin ilk bölümünde, standart x-uzayı yaklaşımında doğrusal olmayan seçme alanı hesaba katılmadığında geriçatılan görüntüde çarpılma oluştuğu gösterilmektedir. Ayrıca, geriçatılan görüntüye etki eden kayma haritası bir kez belirlendikten sonra etkili bir şekilde çarpılma artefaktının ortadan kaldırılabileceği gösterilmektedir. Düzeltilen görüntü, seçim alanı gradyanlarındaki bozulma nedeniyle tarayıcının merkezinden uzak bölgelerde çözünürlük kaybı yaşasa da, nanoparçacıkların konumlarını doğru bir şekilde yansıtmaktadır. MPG'de nanoparçacıkların relaksasyon davranışı, nanoparçacık karakteristikleri veya viskozite ve sıcaklık gibi lokal ortam özellikleri hakkında çıkarımlar yapmak için de kullanılabilir. Nanoparçacık sinyali sürücü alanı (SA) parametreleriyle de değiştiği için, nicel haritalama uygulamalarındaki potansiyel bir problem bu parametrelerin de optimizasyonudur. Bu tezin ikinci kısmında, nanoparçacıkların farklı ortamlardaki kendilerine özgü tepkilerini karakterize etme amaçlı yeni bir hızlandırılmış yaklaşım önerilmektedir. "Manyetik Parçacık Parmak İzi Tanıma" adı verilen bu yöntem, gevşeme izini hızlı bir şekilde geniş bir aralıktaki SA parametrelerini tarayarak numunenin özgün relaksasyon parmak izini haritalamaktadır. Bu yöntem, birkaç parametrenin (örneğin viskozite, sıcaklık, nanoparparçacık tipi, vb.) eşzamanlı haritalanmasını önemli ölçüde kısaltılmış tarama süresinde sağlayabilir.

Anahtar sözcükler: manyetik parçaçık görüntüleme, manyetik nanoparçacıklar, artefaktlar, nanoparçacık karakterizasyonu, haritalama.

Acknowledgement

Firstly, I would like to thank my supervisor, Assoc. Prof. Emine Ülkü Sarıtaş for her guidance and support throughout my years in Bilkent as an undergraduate and as a master's student. She was the person illuminated my interest in medical imaging in her course and she ended up being the reason that I chose to pursue my master's degree in Bilkent. During my master's I learned so much from her about the field I was working, about academic life. For me, it was inspiring to work with her. I truly see her as a role model especially considering the unfortunate scarcity of women in STEM fields.

I would like to thank Dr. Can Barış Top for co-advising me in this thesis and also for his direct contribution in the second part of the thesis. He is such a nice person to work with and even though due to outbreak our experimental work was interrupted, I had a chance to work with him and learned several practical tips.

I want to thank Prof. Ergin Atalar for being in my thesis committee as well as his support and guidance that I benefited both as a student in his course and also in our off-discussions.

I would like to thank Asst. Prof. Yeşim Serinağaoğlu Doğrusöz for being in my thesis committee and for her evaluations. I believe with valuable feedbacks from the committee, this thesis is more complete.

I would like to thank the Scientific and Technological Research Council of Turkey for supporting the work in this thesis through TUBITAK Grants 115E677 and 217S069.

I would like to thank my colleagues in our research group: Mustafa Ütkür, Rahmi Çağıl, Ömer Arol, Musa Tunç Arslan, Semih Kurt, Ali Alper Özaslan, Elif Aygün, Bahadır Alp Barlas, Abdallah Zaid Alkilani. They are such great people to work with. I especially would like to thank Mustafa and Rahmi for their help in lab. And all of them for their valuable discussions as well as friendships and off-discussions that I highly value and enjoy. I would like to thank everyone in UMRAM. Even though due to quarantine and social distancing practices, it has been a while that we could spend time in UMRAM, thank all of you for my time in there.

And I would like to thank my friends, who made my life more fulfilling. Firstly, my two best and longtime friends Rümeyza Dinçer and Başak Görüşün. Even though, some distance came along, I know I can depend on these two amazing ladies! I would like to thank Merve Çetiner, Sezen Buse Özgür, Cansu Kömeç, Seçil Eda Doğan, and Gülce Pulat. Bilkent was much more enjoyable for me because of their friendship. I would like to thank Ömer Arol, Abdulsamet Dağaşan for their company especially in these challenging quarantine times. I want to thank several good friends in EE that over the years we spent quiet some time together either in as TAs, being in same project groups or as neighbors in Bilkent housings: Ömer Arol, Abdulsamet Dağaşan, Muzaffer Özbey, Ahmet Safa Öztürk, Rahmi Çağıl, Yunus Erdem Aras, Mahmut Can Soydan, Doğan Kutay Pekcan, Dilan Öztürk.

I would like to thank my family. Firstly, my parents, Canan Karaçalı and Mehmet Yağız for their endless support and love. They always believed in me when I couldn't do most of the times and always supported every decision I made. My gratitude for them is beyond the words. And I would like to thank my dear brother, Haktan. He is definitely the most colorful person I have ever met and I am quite thankful that he is a part of my life. I only wish the best for him.

And finally, I would like to thank Bilal Taşdelen who is my "bestest" friend, the most valuable co-worker and he recently became my husband. He is the joy of my life and I am a better person and a better engineer because of him. He was always there for me when I was down. I am looking for many years to come with him.

Contents

1 Introduction **1**

2 Principles of MPI **4**

2.1 Signal Acquisition 4

2.2 X-Space MPI 7

2.3 Multidimensional X-Space MPI 8

2.4 Relaxation in MPI 10

2.4.1 Direct Estimation of Relaxation Time Constant 11

3 Non-ideal Selection Field Induced Artifacts in X-Space MPI **14**

3.1 Background 14

3.2 Methods 15

3.2.1 Magnetic Field Simulations 16

3.2.2 Imaging Simulations 18

3.2.3 Displacement Map Calculations 19

3.2.4 Unwarping via Displacement Map 21

3.2.5 Resolution Loss Calculations 22

3.2.6 Comparison to Direct Reconstruction 23

3.3 Results 24

3.3.1 Warping Artifact 24

3.3.2 Displacement Map Results 24

3.3.3 Resolution Loss Results 27

3.3.4 Unwarping Results 28

3.3.5 Direct Reconstruction Results 28

3.3.6 Demonstration on a Vasculature Phantom 30

3.4 Discussion 32

4 Magnetic Particle Fingerprinting using Arbitrary Waveform Relaxometer 35

4.1 Background 35

4.2 Methods 37

4.2.1 Rapid Excitation Space Coverage 37

4.2.2 In-house Arbitrary Waveform Relaxometer Setup 39

4.2.3 Overall System 40

4.2.4 System Model in LTSpice 42

4.2.5 Sample Preparation 43
4.2.6 Magnetic Particle Fingerprinting Experiments 44
4.3 Results 45
4.3.1 Excitation Space Coverage 45
4.3.2 Magnetic Particle Fingerprinting Experiments 48
4.4 Discussion 53

5 Conclusions 54

List of Figures

2.1 a) Magnetization M curve of SPIOs vs. the magnetic field amplitude H. Here, H_D represents the sinusoidal drive field. The red curve shows the total field in the FFP, and the blue curve shows that in the saturated regions due to selection field. b) The magnetization M curve as a function of time t. The red curve shows the magnetization response in the FFP and the blue curve shows that in the saturation region. c) Received signal via inductive coil. The first row is the signal from the FFP and there is no received signal from the saturation region. d) Frequency content of the received signal. The signal is expected to be at the harmonics of the applied fundamental frequency f_0. 5

2.2 A typical MPI scanner schematic. Here, the selection field coils are generally permanent magnets that create the selection field within the volume of the scanner (represented by the red magnetic field lines). Then, there are drive field coils which apply the time-varying drive field to excite the nanoparticles inside the scanner. The receive coils are aligned in the same direction and inductively receive the nanoparticle signal. 6

2.3 a) One period of signal corresponding to the actual measurement of Nanomag-MIP at viscosity level 0.89 mPa.s under 6.1 kHz and 12.8 mT magnetic field. The positive half cycle is shown in blue and the negative half cycle is shown in red dashed curve. b) The positive and the negative half cycles are plotted together. Here the negative half cycle is time reversed and the mirror symmetry is taken. The effect of relaxation can be seen as the break in the mirror symmetry of the half cycles. c) After TAURUS algorithm took place, the positive and the negative half cycles are shown on top of each other. It can be seen that after deconvolving with the estimated relaxation kernel the mirror symmetry is restored. . . . 13

3.1 a) In-house FFP MPI scanner with $(2.4, 2.4, -4.8)$ T/m selection field, on which the magnetic field simulations were based. b) The selection field was generated using two permanent disk magnets with 7-cm diameter and 2-cm thickness. For imaging simulations, a 2D phantom with point sources was placed at the center of the magnet configuration at z = 0 plane. 16

3.2 Selection fields in x-, y-, and z-directions at z = 0 plane, a) for the ideal case with constant G_{xx}, G_{yy}, and G_{zz}, and b) for the non-ideal case based on the FFP scanner in Fig. 3.1. c) The corresponding selection field gradients for the non-ideal case at z = 0 plane. The non-linearity of the selection field and the degradation in gradients are visible in regions away from the scanner iso-center. 17

3.3 a) The FOV is partitioned into ROIs with size $p \times p$ mm^2, which are used one at a time. A point source SPIO is placed in the center of the selected ROI. b) Image from the red patch (selected ROI) for the case of ideal selection field. The red cross indicates the peak intensity position. c) Reconstructed image of the same patch for the case of non-ideal selection field. Here, the blue cross indicates the peak intensity position, while the red cross marks the same position as in (b). Δx and Δy are the distances between these two crosses in x- and y-directions, respectively. d) The quiver plot of the displacement map across the entire 4×4 cm^2 FOV (shown here for a low-resolution 2×2 mm^2 grid for display purposes). . 19

3.4 a) The FOV is partitioned into ROIs, with a point source SPIO placed at the center of the selected ROI. b) Image from the red patch for the case of ideal selection field. The blue lines indicate the FWHM measurements, with the corresponding values provided in green. c) The reconstructed image in the case of non-ideal selection field. The FWHM measurements yield similar values as in the ideal case. d) The corrected image after unwarping displays a loss in resolution in both directions. 22

3.5 a) Phantom with point source SPIOs placed at 10 mm separations. b) Image for the ideal selection field, and c) x-space reconstructed MPI image for the case of non-ideal selection field. 24

3.6 a) Theoretical and b) simulated displacement maps in x-direction, and c) theoretical and d) simulated displacement maps in y-direction. Here, the theoretical values were computed via Eqn.3.6, and simulated values were computed as described in Fig.3.3. . . . 25

3.7 a) Theoretical and b) simulated resolution maps in x-direction, and c) theoretical and d) simulated maps in y-direction. The theoretical maps were computed using Eqns. 3.7 and 3.8, and the simulated maps were computed as described in Fig. 3.4. 27

3.8 Results of 3^{rd} degree polynomial fitting for the displacement maps in a) x-direction and b) y-direction. The black marks indicate the measured results at the simulated grid locations. c) The corrected version of the image in Fig. 3.5c, after unwarping using the fitted displacement maps. 29

3.9 The line-by-line scan trajectory for the case of a) ideal selection field and b) non-ideal selection field, showing every fifth line. The targeted FOV was 4×4 cm^2 (marked with the dashed red square). In the non-ideal case, the trajectory warps in regions away from the scanner iso-center, extending outside the intended FOV. c) The direct x-space reconstructed image using the actual FFP trajectory closely matches the corrected image in Fig. 3.8c. 30

3.10 a) A vasculature phantom extending beyond the targeted 4×4 cm^2 FOV (dashed red box). b) Image for the ideal selection field, c) x-space reconstructed image for the non-ideal selection field, and d) corrected image after unwarping. 31

4.1 a) Excitation space consisting of $\left(B_{peak}, f_0\right)$ pairs. The red dots show that only a few frequencies can be used in typical quantitative MPI studies. b) An example linear trajectory in excitation space. Here, the frequency f_0 is kept constant and the B_{peak} values are traversed in the range of interest. c) Another example linear trajectory in excitation space. Here, the B_{peak} value is kept constant and the frequency is traversed in the range of interest. d) A spiral trajectory in excitation space. Note that, with this approach a wider range of $\left(B_{peak}, f_0\right)$ pairs are covered in a single experiment. 37

4.2 a) Spiral trajectory in excitation space. b) The DF waveform constructed using Equation 4.1 with 10 cycles for each sinusoid and $N = 150$. Note that 150 individual experiments are now compressed under 0.5 seconds. 38

4.3 a) In-house AWR setup schematic. b) Actual photograph of the AWR setup. 39

4.4 The schematic for the experimental setup also displaying the brand and model of the lab equipments. 40

4.5 a) An example nanoparticle signal with respect to time. b) The corresponding baseline measurement. Note that each measurement was averaged by two times. 41

4.6 a) Simplified LTSpice model of the hardware setup. Here, V_{in} is the power amplifier and R is its equivalent series resistance. $L_{TX} = 7\ \mu$H is the transmit side inductance of the AWR. Note that the model for the transmit side also includes a series resistance of 2 mΩ. $L_{RX} = 7\ \mu$H is the receive side inductance of the AWR. The receive side is then connected to the LNA, hence terminated with high series impedance. b) The model estimate (blue) and the calibration measurement (red) for the transfer function $H(f) = B_{peak}(f)/V_{in}(f)$, taken using a Hall effect gaussmeter. With this fitted curve, it is possible to obtain desired magnetic field amplitude at a given frequency. 42

4.7 a) Spiral trajectory in excitation space. b) The voltage DF waveform constructed using Equation 4.2 where V_{in}'s are found through Fig. 4.6b with 10 cycles for each sinusoid and $N = 150$. c) The magnetic field corresponding to the voltage DF seen in (b). 43

4.8 a) The drive field $B_d(t)$ corresponding to the spiral trajectory in excitation space. Here, note that the measurement took place via a current probe, then the magnetic field was found. b) LTSpice model estimate for the drive field $B_d(t)$. Here, the current through the inductor L_{TX} (Figure 4.6a) was simulated, then the magnetic field is calculated. Note that, the measurement and the model estimate agree quite well. 46

4.9 a) The drive field $B_d(t)$ (s) corresponding to the linear trajectory in excitation space (constant f_0). Same procedure was applied as in Figure 4.8. b) LTSpice model estimate for the drive field $B_d(t)$. Note that, the measurement and the model estimate agree quite well. 47

4.10 a) The drive field $B_d(t)$ (s) corresponding to the linear trajectory in excitation space (constant B_{peak}). Same procedure was applied as in Figure 4.8. b) LTSpice model estimate for the drive field $B_d(t)$. Note that, the measurement and the model estimate agree quite well. 48

4.11 The product of $B_{peak} \times f_0$ corresponding to a) the linear trajectory in which B_{peak} is kept constant, b) the linear trajectory in which f_0 is kept constant, and c) the spiral trajectory. Note that the product oscillates in (c), creating a duty cycle effect and preventing the coil from heating up, whereas in (a) and (b) the product increases throughout the trajectory. 49

4.12 a) 3-D plot of the τ-fingerprint for the Nanomag-MIP at 0.89 mPa.s for different trajectories. b) 3-D plot of the normalized τ-fingerprint. The normalization is done with the respective periods. 49

4.13 a) 3-D plot for the τ-fingerprints for the Nanomag-MIP at 0.89 mPa.s (blue) and at 5.04 mPa.s (red). b) 3-D plot for the normalized τ-fingerprints. Here note that in both plots the responses are quite similar, and the ability to distinguish increases when the peak magnetic field B_{peak} decreases and/or the frequency f_0 decreases. . 50

4.14 a) 3-D τ-fingerprint plot for the Nanomag-MIP (blue) and Perimag (red). Both samples were at 0.89 mPa.s viscosity. b) 3-D plot for the normalized τ curves of the Nanomag-MIP (blue) and the Perimag (red) samples. Note that for better visualization, 4^{th} order median filtering was applied on the curves. 50

4.15 a) 3-D τ-fingerprint plot for the Synomag-D (blue), Vivotrax (red), and Perimag (yellow). All samples were at 0.89 mPa.s viscosity level. b) 3-D plot for the normalized τ. c) The 3-D plot seen in (a) is rotated for better visual separation of τ-fingerprints of the nanoparticles. d) Rotated version of the normalized τ-fingerprint seen in (b). Note that for better visualization 4^{th} order median filtering was applied. 51

4.16 Significance test results presented as a bar chart. It can be seen that the pairs Nanomag-MIP - Vivotrax, Nanomag-MIP - Synomag and Vivotrax - Synomag are significantly different. As shown in Figure 4.14 the response of Nanomag-MIP and Perimag are found to be similar to each other. 52

List of Tables

4.1 Prepared samples at 2 different viscosity levels 44

Chapter 1

Introduction

Magnetic Particle Imaging (MPI) is a novel tomographic imaging modality that was first proposed in 2005 and has been rapidly developing since then [1]. It offers superb resolution (theoretically sub-millimeter resolution), high-contrast, and high sensitivity [1, 2, 3, 4]. MPI utilizes the non-linear magnetization curves of superparamagnetic iron oxides (SPIOs) for imaging. The tracers used in MPI are shown to be safe to administer to human subjects, even for patients with Chronic Kidney Disease (CKD). Moreover, there is no ionizing radiation neither from the scanner nor from the tracer, which makes MPI a safe alternative to imaging modalities such as positron emission tomography (PET) or computed tomography (CT). MPI offers a diverse array of applications such as angiography [4, 5], cancer imaging [6], and stem cell tracking [7, 8, 9].

In MPI, a static magnetic field called a selection field is created by placing two strong magnets with the same poles facing each other. In this field, there exists a field-free-region (FFR) that can be either a field free point (FFP) or a field free line (FFL) depending on the configuration of the magnets. This FFR is scanned through the object of interest via a time-varying magnetic field called a drive field. MPI detects the response of the SPIOs to the applied external magnetic fields with no signal from the background tissue itself. After the signal is acquired, there are two main approaches to reconstruct an image: system function reconstruction

(SFR) and x-space MPI. In the SFR approach, the entire MPI system is treated as a black box and by means of calibration measurements the MPI image (i.e., the nanoparticle distribution in space) is reconstructed by solving an inverse problem [10]. In x-space MPI, on the other hand, imaging is treated as scanning in spatial domain [11]. One of the important assumptions here is that the gradient of the selection field is constant throughout the imaging volume, which makes the traversing FFR position unique in space, with a constant resolution across the imaging volume.

However, it is often the case that such ideal fields only hold for a small volume in space, and beyond which undesired deviations can occur. It is important to understand the type of the artifacts in the resulting image when the reconstruction stage does not account for non-idealities. With this understanding, artifacts can be addressed or prevented either partially or totally in the first place by considering the trade-off between image quality and hardware design parameters. In Chapter 3, this study is done for the selection field. A warping artifact together with a resolution loss are shown and a remedy for the warping artifact is presented together with a consideration for the design process of a scanner.

Another important assumption often done in MPI is the adiabatic assumption, i.e., the response of the nanoparticles are assumed to be instantaneous with the applied magnetic field. In reality, however, the response of nanoparticles depends on local environmental conditions such as the viscosity of the medium, the temperature, the binding state of the nanoparticle [12], as well as the drive field parameters, i.e., magnetic field amplitude and frequency [13]. While the adiabatic assumption makes modeling convenient, the aforementioned dependence on local environment leads to promising applications such as viscosity and/or temperature mapping, which can then be utilized for diagnostic purposes (such as hypertension and cerebral infarction) [14, 15, 16].

While mapping the magnetization response of nanoparticles under different conditions leads to valuable insights for many practical applications, predicting this response via simulations is rather difficult. Therefore, experiments under different drive field parameters are needed to determine the optimal values, which can be impractical in standard resonant MPI systems. In Chapter 4, a novel approach named "*Magnetic Particle Fingerprinting*" is presented. This approach rapidly covers the "*excitation space*" (i.e., the space consisting of amplitude and frequency of the drive field) using a non-resonant system and maps the nanoparticle characteristics under different environmental conditions. This framework enables distinguishing different nanoparticles, viscosities, temperatures via the unique responses of the nanoparticles. Furthermore, the acquired signal database can be used to optimize the drive field parameters for a specific imaging type/application considering the nanoparticle at hand.

Chapter 2

Principles of MPI

2.1 Signal Acquisition

MPI utilizes SPIOs for imaging and the very characteristics of these nanoparticles that enables imaging is modeled by the Langevin function [1, 11]. As seen in Figure 2.1a beyond a certain threshold of magnetic field, the magnetization is saturated. In a typical MPI scanner (depicted in Figure 2.2) two magnets placed with the same poles facing each other create a static magnetic field with zero strength in the center. This point is called the field free point (FFP). The nanoparticles residing outside the vicinity of the FFP experience a non-zero magnetic field and become saturated. When the nanoparticles in the FFP experience a sinusoidal drive field, the time-varying magnetization of the nanoparticles induce a signal in the receive coil. In contrast, there is no signal contribution from nanoparticles in other regions since their magnetizations remain at saturation (see Figure 2.1). Moreover, the signal consists of the harmonics of the applied sinusoidal drive field as seen in Figure 2.1d.

The static magnetic field due to permanent magnets is called the selection field, denoted here as $\vec{B}_s(x, y, z)$. As explained above, this field has a zero-field region (field free region, FFR), which can be a FFP or a field free line (FFL) depending

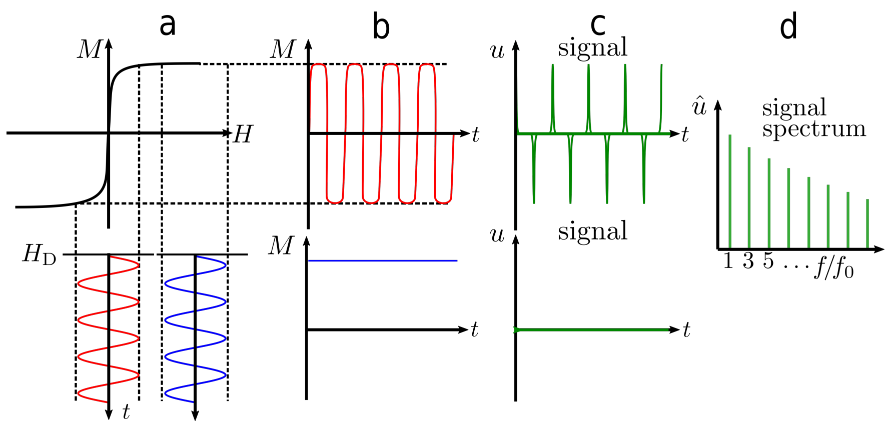

Figure 2.1: a) Magnetization M curve of SPIOs vs. the magnetic field amplitude H. Here, H_D represents the sinusoidal drive field. The red curve shows the total field in the FFP, and the blue curve shows that in the saturated regions due to selection field. b) The magnetization M curve as a function of time t. The red curve shows the magnetization response in the FFP and the blue curve shows that in the saturation region. c) Received signal via inductive coil. The first row is the signal from the FFP and there is no received signal from the saturation region. d) Frequency content of the received signal. The signal is expected to be at the harmonics of the applied fundamental frequency f_0.

on the configuration of the magnets. The selection field can be written as follows for the 1-D case

$$B_s(x) = -Gx \tag{2.1}$$

where $x = 0$ is the position of the FFP and G (T/m) is the selection field gradient strength.

Then, to excite the SPIOs, another magnetic field is applied on top of the selection field. This time-varying field is called the drive field or the excitation field. Denoted here as $B_d(t)$, the drive field is typically purely sinusoidal and can be expressed as:

$$B_d(t) = B_{peak} \cos(2\pi f_0 t) \tag{2.2}$$

Here, B_{peak} (T) is the peak field amplitude and f_0 (Hz) is the fundamental frequency. So, in a given time at a given position, the magnetic field can be expressed

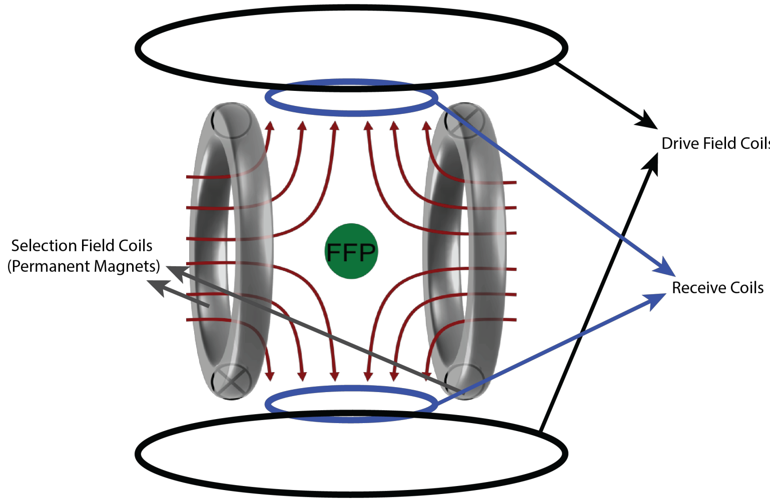

Figure 2.2: A typical MPI scanner schematic. Here, the selection field coils are generally permanent magnets that create the selection field within the volume of the scanner (represented by the red magnetic field lines). Then, there are drive field coils which apply the time-varying drive field to excite the nanoparticles inside the scanner. The receive coils are aligned in the same direction and inductively receive the nanoparticle signal.

as the summation of selection field and drive field, i.e.,

$$\begin{aligned} B(x,t) &= B_d(t) + B_s \\ &= B_d(t) - Gx \end{aligned} \tag{2.3}$$

Here, the location of the FFP can be found by solving $B(x,t) = 0$. Solving Equation 2.4 yields the location of the FFP, x_s (m) as,

$$B(x,t) = 0 \tag{2.4}$$

$$B_d(t) - Gx_s = 0 \tag{2.5}$$

$$x_s(t) = \frac{B_d(t)}{G} \tag{2.6}$$

There are two main approaches to reconstruct an image in MPI once the signal is received: system function reconstruction (SFR) method and x-space reconstruction. In SFR, the MPI system is treated as a black box and the problem is formulated as an inverse problem of a linear system of equations. Before imaging takes place, an extensive calibration is performed using a point source of

SPIOs. In x-space, however, the nanoparticle response can directly be found and mapped using the FFP position and velocity information, which is explained in more detail in the next section.

2.2 X-Space MPI

X-space MPI treats imaging as a spatial scanning process [11, 17]. In this approach, one can directly write the magnetization of the nanoparticles using the Langevin function as seen in Equation 2.7

$$M(H) = m\rho\mathcal{L}(kH) \tag{2.7}$$

where m (Am^2) is the magnetic moment of the nanoparticle, k (m/A) is a property of the nanoparticle, $H = B/\mu_0$ is applied magnetic field, ρ (particles/m^3) is the nanoparticle density. Finally, the Langevin function is

$$\mathcal{L}(x) = \coth(x) - \frac{1}{x} \tag{2.8}$$

Assuming the nanoparticle density is only in the x-direction and FFP position is at $x_s(t)$, the magnetization can be written as [11],

$$M(x,t) = m\rho(x)\delta(y)\delta(z)\mathcal{L}\big(kG(x_s(t) - x)\big) \tag{2.9}$$

Then, the 1D MPI signal can be expressed as follows,

$$\begin{aligned} s_{ideal}(t) &= \int_V B_1 \frac{\partial M(\vec{x},t)}{\partial t} dV \\ &= B_1 \frac{\partial}{\partial t} \int_V M(\vec{x},t) dV \end{aligned} \tag{2.10}$$

where $-B_1$ (T/A) is the coil sensitivity. Using Equation 2.9 here,

$$\begin{aligned} s_{ideal}(t) &= B_1 \frac{\partial}{\partial t} \int\int\int m\rho(u)\delta(v)\delta(w)\mathcal{L}\big(kG(x_s(t) - x)\big) dudvdw \\ &= B_1 \frac{\partial}{\partial t} \big(m\rho(x) * \mathcal{L}\big(kGx\big)\big)|_{x=x_s(t)} \\ s_{ideal}(t) &= B_1 m\rho(x) * \dot{\mathcal{L}}\big(kGx\big)|_{x=x_s(t)} kG\dot{x}_s(t) \end{aligned} \tag{2.11}$$

where $\dot{x_s}(t)$ is the FFP velocity. The MPI image can then be written using Equation 2.11 as,

$$IMG\big(x_s(t)\big) = \frac{s_{ideal}(t)}{B_1 mkG\dot{x_s}(t)} = \rho(x) * \dot{\mathcal{L}}\big(kGx\big)|_{x=x_s(t)} \tag{2.12}$$

In Equation 2.12 the image is expressed as the convolution of the nanoparticle distribution and the point-spread-function (PSF). Here, the PSF for 1-D MPI system can be identified as $h(x) = \dot{\mathcal{L}}\big(kGx\big)$.

2.3 Multidimensional X-Space MPI

Derivations given in Section 2.2 can be extended into multidimensional case using similar concepts [17]. Firstly, the selection field gradient matrix $\boldsymbol{G}$ can be expressed as follows,

$$\boldsymbol{G} = G_{zz}\begin{bmatrix} -\frac{1}{2} & 0 & 0 \\ 0 & -\frac{1}{2} & 0 \\ 0 & 0 & 1 \end{bmatrix} \tag{2.13}$$

Then, a multidimensional drive field can be written as,

$$\vec{B_d}(t) = \begin{bmatrix} B_x(t) \\ B_y(t) \\ B_z(t) \end{bmatrix} \tag{2.14}$$

Using the Equations 2.13 and 2.14, the total magnetic field can be written as,

$$\begin{aligned} \vec{B}(\vec{x},t) &= \vec{B_d}(t) - \boldsymbol{G}\vec{x} \qquad (2.15) \\ &= \begin{bmatrix} B_x(t) \\ B_y(t) \\ B_z(t) \end{bmatrix} - G_{zz}\begin{bmatrix} -\frac{1}{2} & 0 & 0 \\ 0 & -\frac{1}{2} & 0 \\ 0 & 0 & 1 \end{bmatrix}\begin{bmatrix} x \\ y \\ z \end{bmatrix} \end{aligned}$$

The instantaneous FFP position $\vec{x_s}(t)$ can be found by setting $\vec{B}(\vec{x},t) = 0$. That is,

$$\vec{x_s}(t) = \boldsymbol{G}^{-1}\vec{B_d}(t) \tag{2.16}$$

Similarly, the magnetization of the SPIOs can be extended to the multidimensional case,

$$\vec{M}(\vec{H}) = \rho m \mathcal{L}\left[k||\vec{H}||\right]\hat{\vec{H}} \tag{2.17}$$

here, $\hat{\vec{H}} = \vec{H}/||\vec{H}||$. From Equations 2.16 and 2.17, the magnetization density of the nanoparticles with a distribution $\rho(\vec{x})$ can be written as,

$$\vec{M}(\vec{x}, t) = \rho(\vec{x}) m \mathcal{L}\left[k||\boldsymbol{G}(\vec{x_s} - \vec{x})||\right] \frac{\boldsymbol{G}(\vec{x_s} - \vec{x})}{||\boldsymbol{G}(\vec{x_s} - \vec{x})||} \tag{2.18}$$

Defining, the sensitivity matrix for the receive coil in x-, y- and z-axes as $-\boldsymbol{B_1}(\vec{x}) = \begin{bmatrix}\vec{B}_{1x} & \vec{B}_{1y} & \vec{B}_{1z}\end{bmatrix}^T$, the multidimensional signal equation (with some simplifications applied) is obtained as [17],

$$s(t) = \boldsymbol{B_1}(\vec{x}) m \rho(\vec{x}) *** \frac{||\dot{\vec{x}}_s||}{H_{sat}} \vec{h}(\vec{x}) \hat{\dot{\vec{x}}}_s |_{\vec{x} = \vec{x}_s(t)} \tag{2.19}$$

Here, $\hat{\dot{\vec{x}}}_s$ represents the scanning direction and $\boldsymbol{h}(\vec{x})$ is the multi-dimensional PSF [17]:

$$h(\vec{x}) = \dot{\mathcal{L}}\left(\frac{||\boldsymbol{G}\vec{x}||}{H_{sat}}\right) \frac{\boldsymbol{G}\vec{x}}{||\boldsymbol{G}\vec{x}||} \left[\frac{\boldsymbol{G}\vec{x}}{||\boldsymbol{G}\vec{x}||}\right]^T + \frac{\mathcal{L}(\frac{||\boldsymbol{G}\vec{x}||}{H_{sat}})}{\frac{||\boldsymbol{G}\vec{x}||}{H_{sat}}} \left(\boldsymbol{I} - \frac{\boldsymbol{G}\vec{x}}{||\boldsymbol{G}\vec{x}||} \left[\frac{\boldsymbol{G}\vec{x}}{||\boldsymbol{G}\vec{x}||}\right]^T\right) \boldsymbol{G} \tag{2.20}$$

The PSF can be decomposed into two envelopes, called tangential and normal envolopes [17]:

$$ENV_T = \dot{\mathcal{L}}\left(\frac{||\boldsymbol{G}\vec{x}||}{H_{sat}}\right) \tag{2.21}$$

$$ENV_N = \frac{\mathcal{L}\left(\frac{||\boldsymbol{G}\vec{x}||}{H_{sat}}\right)}{\frac{||\boldsymbol{G}\vec{x}||}{H_{sat}}} \tag{2.22}$$

As a one final note, the tangential envelope turns out to be significantly narrower than the normal envelope.

In 3-D x-space MPI theory, the images are produced on an internal reference frame formed by two vectors that are collinear and transverse to the FFP velocity vector [17]. The collinear PSF, $h_{||}(x, y, z)$, is the vector sum of the tangential and normal envelopes and it forms the desired resolution. On the other hand, the transverse PSF, $h_{\perp}(x, y, z)$, is the vector difference of the two envelopes and its magnitude is much smaller than that of the collinear PSF [17].

2.4 Relaxation in MPI

Langevin function modeling the behavior of the nanoparticles under an applied magnetic field is based on the adiabatic assumption, i.e., the nanoparticles can align themselves with the applied magnetic field instantaneously. In practice, however, the received MPI signal is affected by the relaxation behavior of the SPIOs. The relaxation causes a peak shift in the MPI signal together with loss in the signal amplitude, thus blurring the image.

There are two mechanisms that govern the relaxation behavior of the nanoparticles: Brownian and Neel relaxations. These are zero-field models, i.e., they are applicable when an applied static field is removed. Brownian relaxation describes a physical rotation of the nanoparticle so that its magnetic moment aligns externally. Neel relaxation, on the other hand, describes the alignment of the magnetic moment internally with the applied field. The individual relaxation time constant expressions for these mechanisms can be written as,

$$\tau_B = \frac{3\eta V_h}{kT} \tag{2.23}$$

$$\tau_N = \frac{\sqrt{\pi}\beta\big(1\alpha'^2 M_s\big)}{4\gamma\alpha'(\beta K)^{3/2}} \tag{2.24}$$

where τ_B is the zero-field Brownian relaxation time, η is the fluid viscosity, T is the absolute temperature, V_h is the hydrodynamic volume of the particle, and k is the Boltzmann's constant. τ_N is the zero-field Neel relaxation time, M_s is the saturation magnetization, V_c is the core volume, K is the anisotropy constant, α' is the damping constant, γ is the electron gyromagnetic ratio and $\beta = V_c/(kT)$ [13, 18].

In literature, often the effective relaxation time constant is taken to be a parallel process of these two mechanisms i.e.,

$$\tau = \frac{\tau_B \tau_N}{\tau_B + \tau_N} \tag{2.25}$$

However, in reality the process is considerably more complex and the contribution from Brownian and Neel mechanisms change with respect to the viscosity (η), temperature (T), the size of the nanoparticle (V_h, V_c), the applied magnetic field amplitude (B_{peak}), and the magnetic field frequency (f_0).

In literature, there are approaches to model the response of the nanoparticles under time-varying magnetic field with different environmental conditions. One such method is to use Fokker-Planck equations, treating the magnetic moment of the nanoparticles as probability density functions [13]. Even though this model takes the drive field parameters into account, still the Brownian and Neel relaxations are examined separately. Recently, another study is published to model coupled relaxation behavior [18], however, simulating the nanoparticle behavior is still complicated and the simulations need to be verified with extensive experimental work.

Independent from the underlying mechanisms, however, the relaxation effect blurs the MPI signal in asymmetric fashion depending on the scanning direction. It has been shown that the relaxation effect can be incorporated into the x-space derived signal (Equation 2.11) as a time domain convolution as,

$$s(t) = s_{ideal}(t) * r(t) \tag{2.26}$$

where

$$r(t) = \frac{1}{\tau} e^{-t/\tau} u(t) \tag{2.27}$$

Here, $u(t)$ is the Heaviside step function. It has been shown via extensive experimental work that this simple phenomenological model accurately characterizes the MPI response for a wide range of frequencies and drive field amplitudes [19].

2.4.1 Direct Estimation of Relaxation Time Constant

Recently, a study proposed a method called TAURUS (TAU estimation via Recovery of Underlying mirror Symmetry) to estimate the relaxation time constant without any calibration [20, 14]. In MPI, positive and negative half cycles of the drive field move the FFP forward and backward across the scanned partial field of view (FOV). Hence, the ideal MPI signal acquired during the positive and negative scanning directions are mirror symmetric, i.e., positive half cycle and the time-reversed and negated half cycle of the ideal signal are identical, independent from the nanoparticle distribution $\rho(x)$. The ideal half signal can be expressed as,

$$s_{pos,ideal}(t) = -s_{neg,ideal}(-t) = s_{half}(t) \tag{2.28}$$

where $s_{half}(t)$ is the ideal half-cycle signal.

Adding the relaxation effect, the MPI signal is effectively blurred along the scanning direction, thus breaking the mirror symmetry between the two half cycles [21]. In theory, the half cycles would overlap if there is no relaxation. Using the convolution of the ideal signal with relaxation kernel (Equation 2.26), $s_{pos}(t)$ and $s_{neg}(t)$ can be written as,

$$s_{pos}(t) = s_{pos,ideal}(t) * r(t) = s_{half}(t) * r(t) \tag{2.29}$$

$$s_{neg}(t) = s_{neg,ideal}(t) * r(t) = -s_{half}(-t) * r(t) \tag{2.30}$$

Using the model for relaxation kernel $r(t)$ (Equation 2.27), the two equations given for $s_{pos}(t)$ and $s_{neg}(t)$ can be solved simultaneously [20]. The Fourier transform of the kernel and the positive and negative half cycles are,

$$\mathcal{F}\{r(t)\} = R(f) = \frac{1}{\big(1 + i2\pi f\tau\big)} \tag{2.31}$$

$$\mathcal{F}\{s_{pos}(t)\} = S_{pos}(f) = S_{half}(f)R(f) \tag{2.32}$$

$$\mathcal{F}\{s_{neg}(t)\} = S_{neg}(f) = -S_{half}(-f)R(f) \tag{2.33}$$

Here, since $s_{half}(t)$ is real valued, its Fourier transform $S_{half}(f)$ has conjugate symmetry, hence the last equation can be re-written as,

$$\mathcal{F}\{s_{neg}(t)\} = S_{neg}(f) = -S^{*}_{half}(f)R(f) \tag{2.34}$$

Finally, combining the equations given for $R(f)$, $S_{pos}(f)$ and $S_{neg}(f)$ one can obtain the relaxation time constant estimate as,

$$\tau = \frac{S^*_{pos}(f) + S_{neg}(f)}{i2\pi f\big(S^*_{pos}(f) - S_{neg}(f)\big)} \tag{2.35}$$

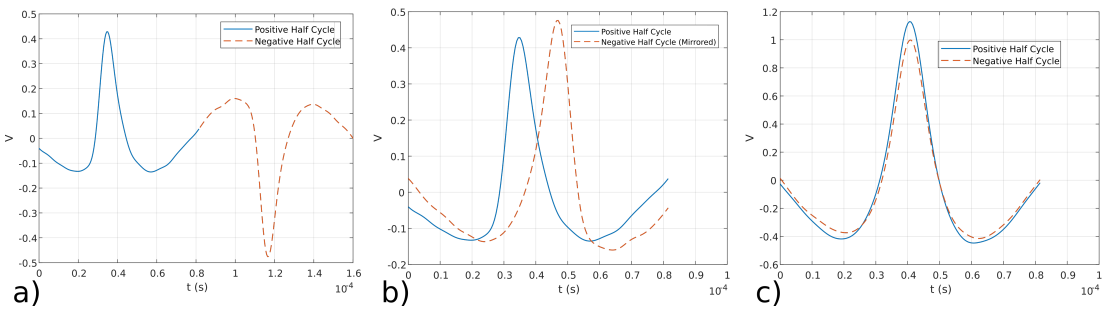

Figure 2.3: a) One period of signal corresponding to the actual measurement of Nanomag-MIP at viscosity level 0.89 mPa.s under 6.1 kHz and 12.8 mT magnetic field. The positive half cycle is shown in blue and the negative half cycle is shown in red dashed curve. b) The positive and the negative half cycles are plotted together. Here the negative half cycle is time reversed and the mirror symmetry is taken. The effect of relaxation can be seen as the break in the mirror symmetry of the half cycles. c) After TAURUS algorithm took place, the positive and the negative half cycles are shown on top of each other. It can be seen that after deconvolving with the estimated relaxation kernel the mirror symmetry is restored.

After the relaxation time constant τ is estimated, the signal can be deconvolved by the relaxation kernel $r(t)$. In theory, deconvolution step recovers the mirror symmetry between the two half cycles. In practice, there may be additional system induced delays (ϕ) in the received signal. Therefore, TAURUS jointly estimates the relaxation time constant and the system delays [20]. The (τ, ϕ) pair is chosen as the solution that minimizes the root-mean-square error (RMSE) between the deconvolved versions of the positive and the mirror negative half cycles. The break in the mirror symmetry due to the relaxation effect and the restoration of it after deconvolving with the relaxation kernel estimated via TAURUS can be seen Figure 2.3 for an actual MPI signal of Nanomag-MIP at viscosity level 0.89 mPa.s under 6.1 kHz and 12.8 mT peak magnetic field.

Chapter 3

Non-ideal Selection Field Induced Artifacts in X-Space MPI

This chapter is based on the publication titled "Non-ideal Selection Field Induced Artifacts in X-Space MPI", E. Yagiz, A.R. Cagil, E. U. Saritas, *International Journal on Magnetic Particle Imaging*, No : 2006001, 2020.

3.1 Background

In MPI, the ideal signal is defined via the response of the nanoparticles to an oscillating drive field [1]. A typical simplifying assumption in MPI is that the selection field gradient is constant in the imaging field-of-view (FOV) [11, 17, 22, 10]. Such highly linear gradient fields could be achieved using large magnets and/or additional coils, e.g., similar to shim coils used in magnetic resonance imaging (MRI) to compensate for B_0 field inhomogeneity [23]. However, practical trade-offs such as the total cost of the system may limit these approaches. For the case of system function reconstruction (SFR), the field non-linearity is implicitly taken into account and corrected, at the cost of a very lengthy calibration procedure that incorporates overscanning [24]. For basic x-space reconstruction, geometric warping effects are expected to occur if the FOV extends beyond the linear region [11].

Similar problems have extensively been investigated in MRI, as the non-linearity of the magnetic field gradients cause what is known as “gradient warping” [25, 26]. In MPI, artifacts due to non-ideal selection fields were previously demonstrated for field free line (FFL) MPI with Radon-based and SFR-based reconstructions, although no solutions were suggested [27].

This chapter presents a simulation-based investigation of selection-field-induced warping and resolution loss for field free point (FFP) MPI with basic x-space reconstruction, together with theoretical derivations of both effects. The results show that the warping effects are relatively benign and can be effectively addressed via unwarping algorithms to achieve a geometrically accurate representation of the underlying nanoparticle distribution. The resolution loss cannot be corrected in such a simple fashion, and may be the factor that determines the maximum size of the FOV for a given scanner setup.

3.2 Methods

Simulations for selection-field-induced-warping were performed in four stages: 1) Magnetic fields were simulated for both the ideal and non-ideal selection field cases. The simulation parameters were based on the in-house prototype FFP MPI scanner that features (2.4, 2.4, -4.8) T/m selection field gradients [28, 21]. 2) Imaging simulations were performed using either the ideal or non-ideal selection fields, followed by x-space MPI reconstruction with DC recovery [5, 29]. 3) The selection-field-induced warping and resolution loss of the MPI image was quantified for each pixel via a displacement map, and compared with theoretical expectations. 4) A potential solution for the warping artifact was implemented via a geometric transformation of the reconstructed images using the displacement maps.

To determine the selection-field-induced resolution loss due to the position-dependent degradation in selection field gradients, images from a non-ideal selection field were investigated with and without image unwarping using the displacement map. To quantify the resolution, full-width-half-maximum (FWHM) values were measured, and compared with values from x-space theory.

The following sections provide details of each step.

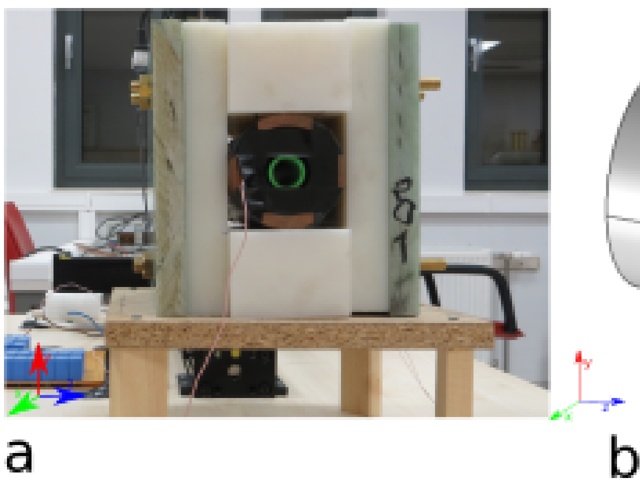

Figure 3.1: a) In-house FFP MPI scanner with $(2.4, 2.4, -4.8)$ T/m selection field, on which the magnetic field simulations were based. b) The selection field was generated using two permanent disk magnets with 7-cm diameter and 2-cm thickness. For imaging simulations, a 2D phantom with point sources was placed at the center of the magnet configuration at z = 0 plane.

3.2.1 Magnetic Field Simulations

Magnetic field values for the selection field, $\vec{B_s}(\vec{x}) = \left(B_x, B_y, B_z\right)$, were calculated for the parameters of the in-house FFP MPI scanner shown in Fig. 3.1a. This scanner has two permanent disk magnets with 7-cm diameter and 2-cm thickness. The separation of the two magnets is 8 cm, with North poles facing each other (see Fig. 3.1b). This prototype scanner has a relatively small region where the selection field is homogeneous. Hence, it is suitable for investigating the warping effects.

For the simulation of ideal selection field, Eqn. 3.1 was used:

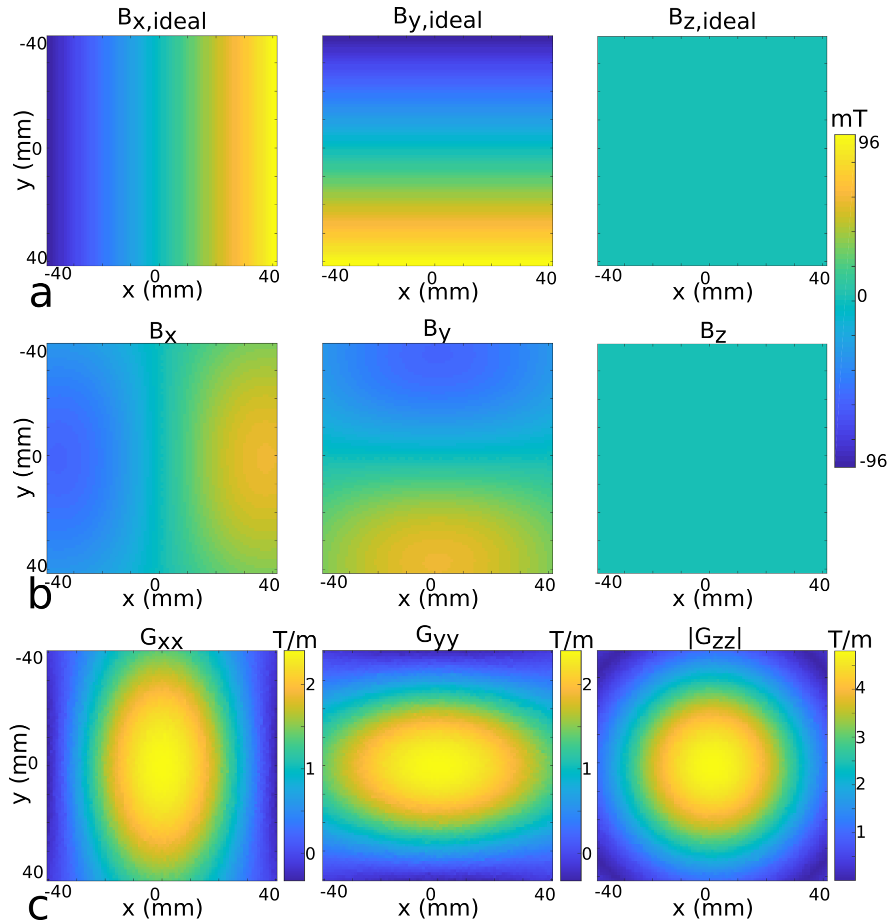

Figure 3.2: Selection fields in x-, y-, and z-directions at z = 0 plane, a) for the ideal case with constant G_{xx}, G_{yy}, and G_{zz}, and b) for the non-ideal case based on the FFP scanner in Fig. 3.1. c) The corresponding selection field gradients for the non-ideal case at z = 0 plane. The non-linearity of the selection field and the degradation in gradients are visible in regions away from the scanner iso-center.

$$\vec{B_s}(\vec{x}) = \mathbf{G}\vec{x} \tag{3.1}$$

Here, $\vec{x}$ is position in space and $\mathbf{G}$ is the gradient matrix. For the ideal case, $\mathbf{G}$ is diagonal with trace$(\mathbf{G}) = 0$. Taking the values at the iso-center of the FFP MPI scanner as reference, $\left(G_{xx}, G_{yy}, G_{zz}\right) = \left(2.4, 2.4, -4.8\right)$ T/m was used. For the non-ideal case, the selection field of the FFP scanner was numerically calculated in an $8 \times 8 \times 8$ cm^3 region-of-interest (ROI) using COMSOL 5.1. Accordingly, the above-mentioned magnet configuration was created in COMSOL, and the fields were computed based on Amperes' Law using the AC/DC Module. The magnet grade was chosen as N38, so that the simulated fields match the measured fields of the in-house FFP MPI scanner at the iso-center [28]. The simulations used a discretization of $\Delta x = 1$ mm, $\Delta y = 1$ mm, and $\Delta z = 2$ mm along the x-, y-, and z-directions, respectively. The simulated magnetic fields and the corresponding gradients in x-, y-, and z-directions are shown in Fig. 3.2, together with the ideal cases, at $z = 0$ plane. The non-linearity of the selection field and degradation in gradients away from the scanner center can be clearly seen. While G_{xx} at the scanner iso-center is 2.4 T/m, it falls down to 1.4 T/m approximately 2-cm away from the center.

3.2.2 Imaging Simulations

Imaging simulations were performed using an in-house MPI simulation toolbox in MATLAB (Mathworks, Natick, MA). The phantom consisted of point source superparamagnetic iron oxide nanoparticles (SPIOs) placed at 10 mm equidistant separations in the FOV. This phantom was then placed at the center of the permanent magnet configuration, as depicted in Fig. 3.1b. The following drive field parameters were utilized: 20 mT at 25 kHz along the x-direction, corresponding to a theoretical partial FOV (pFOV) size of 16.7 mm for the ideal case. Since noise effects were not investigated, a relatively small pFOV overlap percentage of 20% was utilized. A realistic nanoparticle diameter of 25 nm was assumed [30], and relaxation effects were ignored. The overall FOV was 4×4 cm^2 at $z = 0$ plane. The FOV was scanned in a line-by-line fashion along the x-direction, with a spacing of 1 mm along the y-direction. The MPI signal, $s(t)$, was computed using the following [31]:

$$s(t) = \left(\int_{FOV} -\mu_0 \frac{\partial \vec{m}(\vec{x}, t)}{\partial t} c(\vec{x}) dV \right) \cdot \vec{\rho}^R(\vec{x}) \tag{3.2}$$

In the volume integral, $c(\vec{x})$ is the nanoparticle distribution in the FOV, μ_0 is the free space magnetic permeability, and $\vec{m}(\vec{x}, t)$ is the average of the magnetic moment of nanoparticles at position $\vec{x}$ at time t. Also, "$\cdot$" represents dot product operation, and $\vec{\rho}^R(\vec{x})$ is the sensitivity of the receiver coil taken as $(1, 0, 0)$ in this work (i.e., a receive coil sensitive to magnetization changes along the x-axis, with constant homogeneity).

After filtering out the fundamental harmonic of the signal, x-space images were obtained using pFOV-based x-space reconstruction with speed compensation and DC recovery [5, 29]. While the signal computation incorporated selection field non-idealities, the image reconstruction steps ignored them. Hence, an ideal selection field was assumed when computing the instantaneous position of the FFP. For the purposes of this work, the reconstruction process did not involve any image deconvolution steps.

3.2.3 Displacement Map Calculations

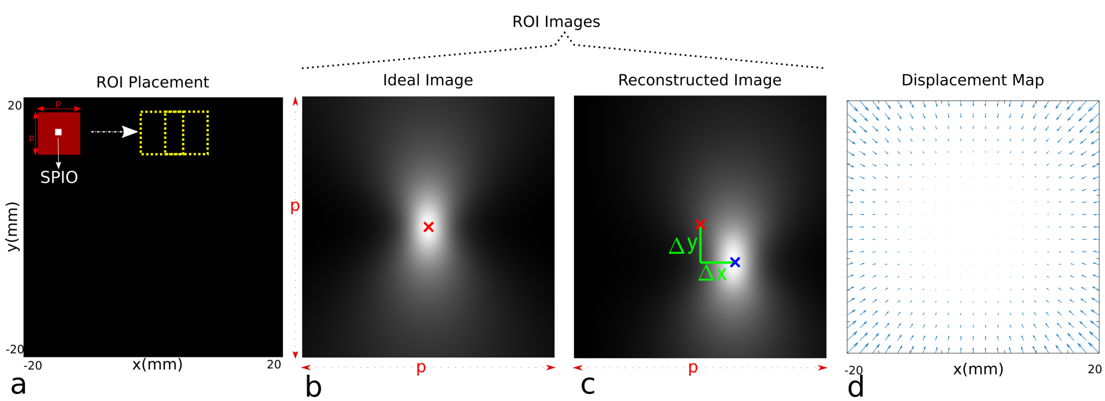

Figure 3.3: a) The FOV is partitioned into ROIs with size $p \times p$ mm^2, which are used one at a time. A point source SPIO is placed in the center of the selected ROI. b) Image from the red patch (selected ROI) for the case of ideal selection field. The red cross indicates the peak intensity position. c) Reconstructed image of the same patch for the case of non-ideal selection field. Here, the blue cross indicates the peak intensity position, while the red cross marks the same position as in (b). Δx and Δy are the distances between these two crosses in x- and y-directions, respectively. d) The quiver plot of the displacement map across the entire 4×4 cm^2 FOV (shown here for a low-resolution 2×2 mm^2 grid for display purposes).

When the underlying selection-field deviates from the ideal case, geometric warping effects are expected to occur.The actual instantaneous position of the FFP can be found by computing the position $\vec{x}$ that satisfies the following equality:

$$\vec{B}_{\text{total}}(\vec{x}, t) = \vec{B}_s(\vec{x}) + \vec{B}_f + \vec{B}_d(t) = 0 \tag{3.3}$$

Here, $\vec{B}_f$ is the focus field and $\vec{B}_d(t)$ is the drive field, both assumed to be homogeneous in space. For the central position of the pFOV, one can use $B_d(t) = 0$. For the case of ideal selection field in Eqn. 3.1, to shift the pFOV center to a desired location $\vec{x}_d$, the following focus field must be applied:

$$\vec{B}_f = -\mathbf{G}\vec{x}_d \tag{3.4}$$

If the same focus field is applied in the case of non-ideal selection field, however, the FFP cannot be shifted by the desired amount. Considering an adjustment to the focus field, the difference between the actual FFP location and the desired FFP location can be found as follows:

$$\vec{B}_s(\vec{x_d}) - \mathbf{G}(\vec{x_d} + \vec{\Delta}) = 0 \tag{3.5}$$

$$\vec{\Delta} = \mathbf{G}^{-1}\vec{B}_s(\vec{x_d}) - \vec{x_d} \tag{3.6}$$

Here, $\vec{B}_s(\vec{x_d})$ is the non-ideal selection field at $\vec{x}_d$, and $\mathbf{G}$ is the ideal gradient matrix with $\text{diag}(\mathbf{G}) = (2.4, 2.4, -4.8)$ T/m in this work. Finally, $\vec{\Delta} = (\Delta x, \Delta y, \Delta z)$ is the amount of the undesired displacement in x-, y-, and z-directions.

To validate the accuracy of this expression, the displacement map is computed by simulating the effect of warping as outlined in Fig. 3.3. First, a small ROI of size 1.2×1.2 cm^2 was selected within the FOV, with a point source SPIO placed at the center of the ROI, as shown in Fig. 3.3a. This ROI was then scanned line-by-line, with imaging parameters kept the same as when scanning the entire FOV. To obtain an image on a finer grid and facilitate FWHM measurements, 2D spline interpolation was applied. An example ideal image for an ROI and the reconstructed image for the non-ideal selection field case are given in Fig. 3.3b-c. Then, the distance between image peak intensity locations were quantified by comparing the resulting patch images, as marked in Fig. 3.3c. This procedure gives the displacements in both x- and y-directions due to the non-ideal field. Next, these steps were repeated by moving the point source SPIO to another grid point, with the ROI positioned around that point. The quiver plot for the resulting displacement map is shown in Fig. 3.3d.

3.2.4 Unwarping via Displacement Map

The warping caused by selection field non-ideality can be corrected using unwarping algorithms. In a real-life implementation, one can either theoretically compute or experimentally measure the displacement map needed for this correction (e.g., by moving a point source sample through the FOV). According to Eqn. 3.6, the undesired displacement solely depends on the selection field and is independent of the nanoparticle type, trajectory, or other imaging parameters. Hence, measuring the displacement map only once on a relatively sparse grid would suffice. In either case, the displacement map is bound to be a coarse map, due to either discretization of the simulation grid or scan time limitations. Here, a 3rd degree polynomial suffices to accurately characterize the displacement in both directions. After polynomial fitting, a much finer displacement map can be used for unwarping the reconstructed image. Here, a geometric transformation was implemented by using MATLAB's built-in *imwarp* function, which takes the reconstructed image and pixel-wise displacement map as the inputs, and outputs the corrected image. This unwarping algorithm finds the corrected intensity at a given pixel through inverse mapping, i.e., by mapping the given pixel location to the corresponding location in the reconstructed image, and computing the pixel intensity via interpolation. This procedure ensures that there will be no gaps or overlaps in the corrected image.

3.2.5 Resolution Loss Calculations

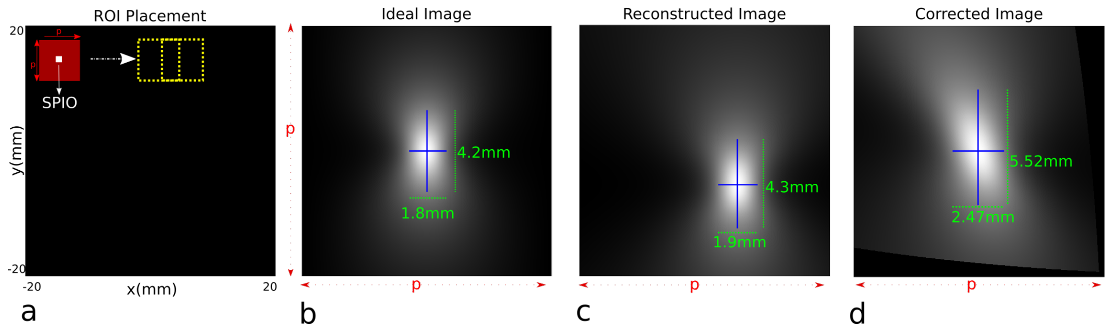

Figure 3.4: a) The FOV is partitioned into ROIs, with a point source SPIO placed at the center of the selected ROI. b) Image from the red patch for the case of ideal selection field. The blue lines indicate the FWHM measurements, with the corresponding values provided in green. c) The reconstructed image in the case of non-ideal selection field. The FWHM measurements yield similar values as in the ideal case. d) The corrected image after unwarping displays a loss in resolution in both directions.

The resolution in x-space MPI changes linearly with the term G^{-1} and is anisotropic [11, 17]. It was shown that the resolution in the tangential direction (i.e., the direction in which the drive field is applied) is better than the resolution in the normal direction (i.e., the direction orthogonal to the drive field). In this work, the tangential and normal directions correspond to x- and y-directions, respectively. Accordingly, the FWHM resolutions for these two directions can be approximated as [17]:

$$\text{FWHM}_x \approx \frac{25 k_B T}{\pi M_{\text{sat}}} G_{xx}^{-1} d^{-3} \tag{3.7}$$

$$\text{FWHM}_y \approx \frac{57 k_B T}{\pi M_{\text{sat}}} G_{yy}^{-1} d^{-3} \tag{3.8}$$

Here, k_B is Boltzmann's constant, T is absolute temperature, d is the nanoparticle diameter, and M_{sat} is the saturation magnetization of the nanoparticle. For the ideal selection field case, the gradient values of $G_{xx} = 2.4$ T/m and $G_{yy} = 2.4$ T/m correspond to theoretical resolutions of $\text{FWHM}_x = 1.8$ mm and

$\mathrm{FWHM}_y = 4.2$ mm, respectively. In the non-ideal case, however, both gradient values change with position, yielding a position-dependent resolution inside the FOV. More specifically, the resolution worsens in both directions in regions away from the scanner iso-center due to the degradation in selection field gradients (see Fig. 3.2c). Still, the resolution at a given position can be computed via Eqns. 3.7 and 3.8 using the actual gradient values at that position. These gradients can be computed from a measured or simulated selection field map via partial derivatives, i.e., $G_{ii} = \partial B_{s,i}/\partial i$, where i is x or y.

To validate the expressions in Eqns. 3.7 and 3.8, the resolution maps of ideal, reconstructed, and corrected images were computed using the approach outlined in Fig. 3.4. Following a similar approach as in the displacement map computation, a point source SPIO was placed at a predetermined grid location. In the same fashion as before, the ideal image and reconstructed image were obtained. This time, the reconstructed image was also corrected using the displacement map. Then FWHM values in both x- and y-directions were measured as shown in Fig. 3.4b-d. This procedure was repeated at all grid locations to obtain position-dependent resolution maps. Interestingly, the reconstructed image displays a point source with almost identical FWHM value as in the ideal case. The resolution loss is only visible in the corrected image after unwarping.

3.2.6 Comparison to Direct Reconstruction

The above-mentioned x-space reconstruction first ignored selection field non-ideality, then corrected its effects via unwarping the reconstructed image. For comparison purposes, a direct x-space reconstruction was also performed by computing the actual FFP position at all time points, i.e., by numerically computing $\vec{x}$ that satisfies $\vec{B}_{\text{total}}(\vec{x}, t) = 0$. To obviate the need for DC recovery, the fundamental harmonic was not filtered out in these simulations. Next, the speed-compensated MPI signal was assigned to actual FFP positions, followed by scattered interpolation to obtain a 2D image on a Cartesian grid.

3.3 Results

3.3.1 Warping Artifact

The x-space MPI images of a 2D phantom shown in Fig. 3.5a are obtained under ideal and non-ideal selection fields. The resulting images are given in Fig. 3.5b and Fig. 3.5c, respectively. In the “reconstructed image”, i.e., the image due to non-ideal selection field, the point sources are misregistered, resulting in an apparent warping. This effect manifests itself more dramatically when the samples are further away from the center of the scanner. The point sources lying at the edges of the FOV are pushed towards the center, as indicated by the red arrows. Hence, if there were SPIOs outside but close to the edge of the FOV, they would have been mapped to positions inside the FOV due to this warping.

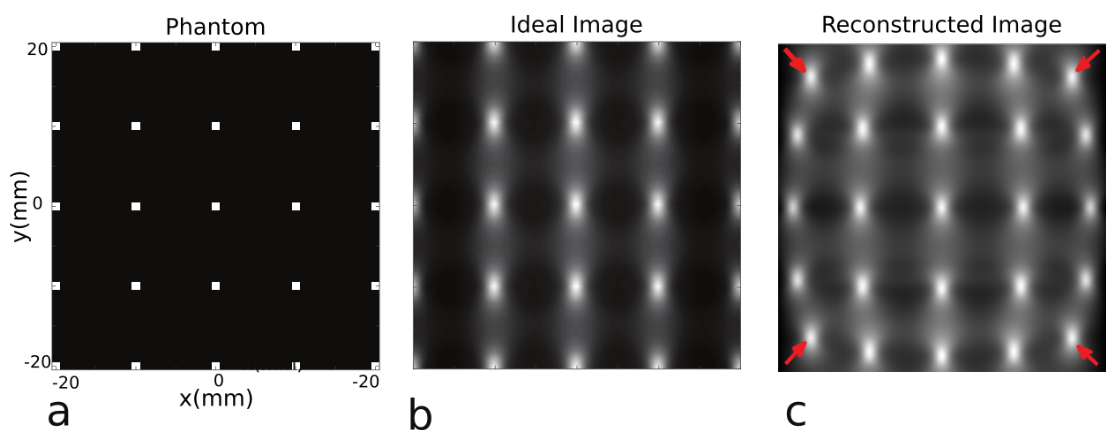

Figure 3.5: a) Phantom with point source SPIOs placed at 10 mm separations. b) Image for the ideal selection field, and c) x-space reconstructed MPI image for the case of non-ideal selection field.

3.3.2 Displacement Map Results

The result of the displacement map calculations are given in Fig. 3.6 for both the theoretical displacements computed using Eqn. 3.6 and for simulated displacements calculated as outlined in Fig. 3.3. The first thing to note is that there is negligible displacement at central locations. The displacement increases away from the center of the scanner, as the field deviates from the ideal case. At the corner of the 4 $\times$ 4 cm^2 FOV, the displacement is around 4 mm in both x- and y-directions, corresponding to approximately 5.7 mm displacement along the diagonal direction. Importantly, the displacements are such that the points are always pushed towards the center of the scanner. In other words, a non-ideal selection field causes us to actually scan a wider FOV than intended, which implies that a corrected image of the targeted FOV can be achieved after unwarping.

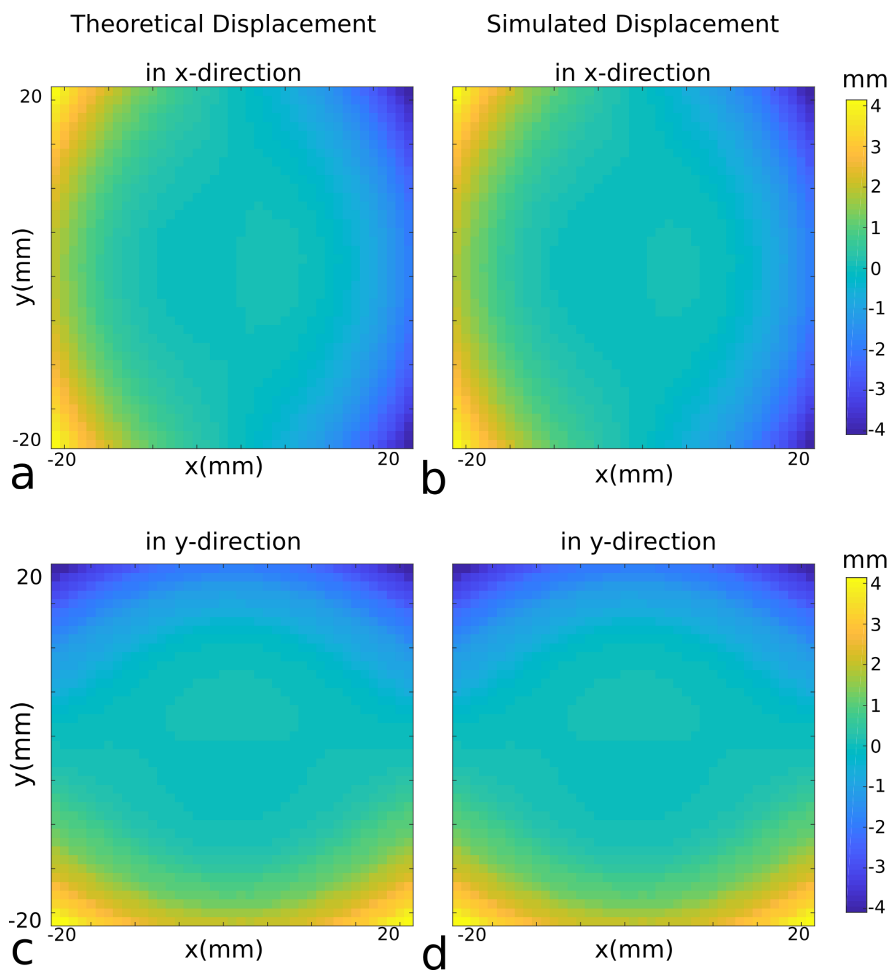

Figure 3.6: a) Theoretical and b) simulated displacement maps in x-direction, and c) theoretical and d) simulated displacement maps in y-direction. Here, the theoretical values were computed via Eqn.3.6, and simulated values were computed as described in Fig.3.3.

Another important result of Fig. 3.6 is that the theoretical and simulated displacements agree excellently, aside from negligible errors stemming from discretization. The normalized root-mean-square errors (NRMSE) between the theoretical and simulated cases are 2.7% and 5.2% for displacements in x- and y-directions, respectively (calculated across the displayed maps in Fig. 3.6). Hence, in a real-life scenario, if one knows the magnetic field map for the selection field, there would not be a need to perform a calibration measurement to determine the displacement map. The selection field map could be computed using simulation tools such as COMSOL (as done in this work) or using analytical expressions that exploit the symmetry of the magnet configuration [32]. Alternatively, as is standard practice in MPI, one can directly measure the selection field map (e.g., using Hall effect probes) [28, 33].

3.3.3 Resolution Loss Results

Fig. 3.7 gives the results of the resolution map for both the theoretical case computed using Eqns. 3.7 and 3.8, and for the simulated case explained in Fig. 3.4. Here, the values for the simulated case correspond to the FWHM resolutions measured after unwarping. The theoretical and simulated cases agree quite well, except for ringing-like features seen in the simulated resolution maps, which potentially stem from FWHM measurements in a discretized setting. The NRMSEs between the theoretical and simulated cases are 2.3% and 4.3% for resolutions in x- and y-directions, respectively (calculated across the displayed maps in Fig. 3.7).

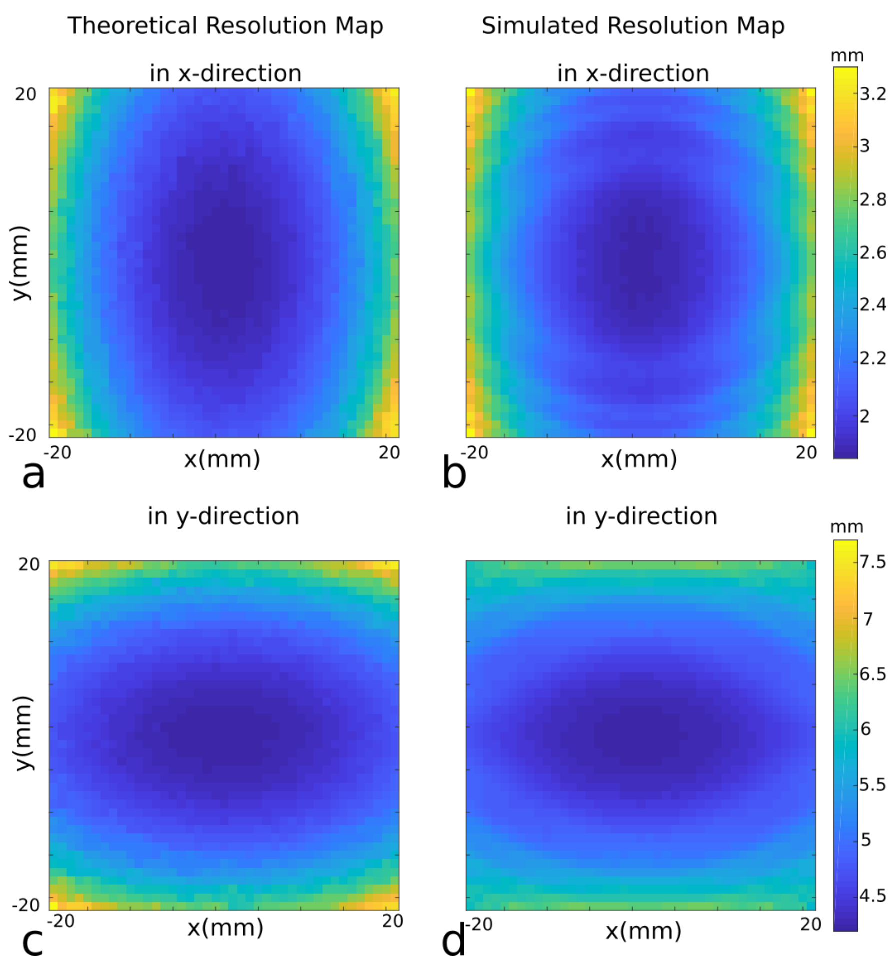

Figure 3.7: a) Theoretical and b) simulated resolution maps in x-direction, and c) theoretical and d) simulated maps in y-direction. The theoretical maps were computed using Eqns. 3.7 and 3.8, and the simulated maps were computed as described in Fig. 3.4.

As expected, the resolutions at the center of the scanner are 1.8 mm and 4.2 mm along the x- and y-directions, respectively. The resolution worsens away from the center of the scanner. At the corner of the 4×4 cm^2 FOV, the simulated resolutions are 3.3 mm and 6 mm in x- and y- directions, respectively.

3.3.4 Unwarping Results

The 3rd degree polynomial fitting to the individual displacement maps are shown in Fig. 3.8a and b. The black marks indicate the measured results at the grid locations. Since magnetic fields do not change abruptly, the displacements are also smooth and slowly changing functions.The NRMSEs between the fitted and measured displacements are 2.4% and 5.1% in x- and y-directions, respectively, verifying that a 3rd degree polynomial with 9 coefficients suffices to describe these smooth functions. With the finer displacement map obtained after polynomial fitting, a corrected image of the 2D phantom is obtained, as shown in Fig. 3.8c. In the corrected image, the point sources positioned at the edges of the FOV are all mapped back to their original positions. As expected, there is a loss of resolution towards the edges of the FOV. Note that this resolution loss is not induced by the unwarping algorithm, but is caused by the non-ideality in selection field gradients, as discussed in Section 3.2.5 and in Section 3.3.3.

3.3.5 Direct Reconstruction Results

To validate that the resolution loss in Fig. 3.8c is not caused by the unwarping algorithm, a direct x-space reconstruction was performed by computing the actual FFP position at all time points. First, Fig. 3.9a-b shows how the line-by-line scanning trajectory is warped in the non-ideal selection field case, extending beyond the targeted FOV. Figure 3.9c displays the direct x-space reconstructed image, in the region corresponding to the intended FOV. This image closely matches the corrected image in Fig 3.8c, verifying that it is the non-ideality of the selection field that causes the loss of resolution towards the edges of the FOV.

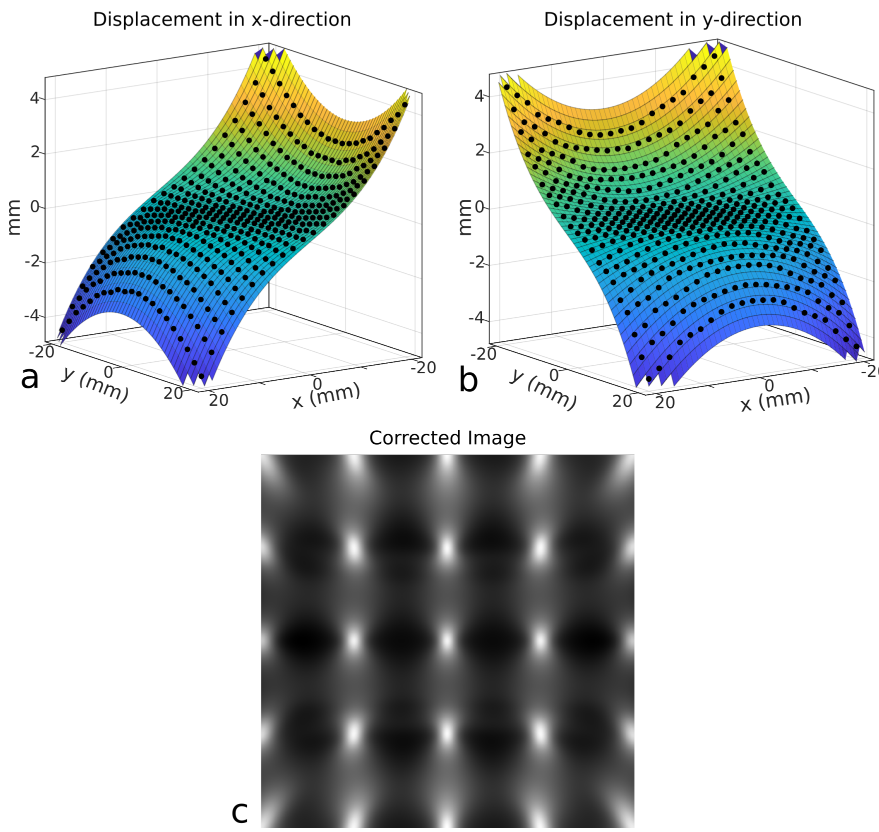

Figure 3.8: Results of 3^{rd} degree polynomial fitting for the displacement maps in a) x-direction and b) y-direction. The black marks indicate the measured results at the simulated grid locations. c) The corrected version of the image in Fig. 3.5c, after unwarping using the fitted displacement maps.

In the ideal trajectory, the drive and receive directions are collinear (i.e., both are along the x-axis), and hence the MPI signal is governed by the collinear point spread function (PSF) only [17]. On the other hand, the warped trajectory causes the receive coil along the x-axis to pick up an MPI signal that has contributions from both the collinear and the transverse PSFs, where the latter is known to induce blurring along the diagonal directions [17, 34]. Note that the contribution of the transverse PSF increases as the trajectory curves further away from the x-axis, leading to a noticeable diagonal blurring towards the corners of the FOV.

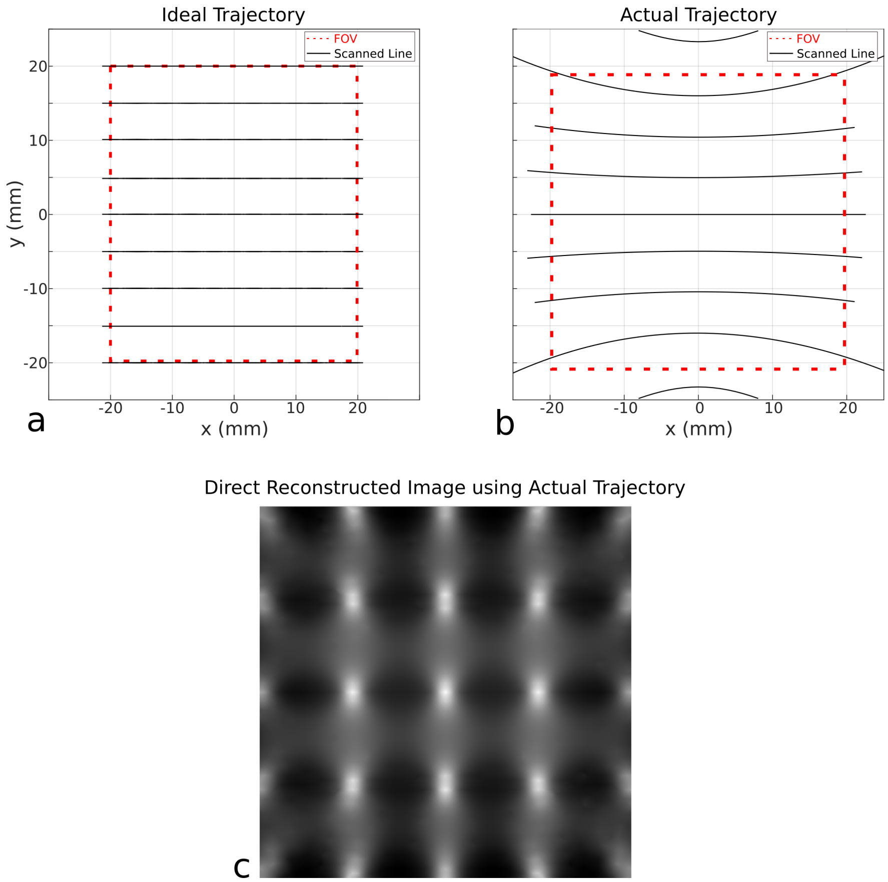

Figure 3.9: The line-by-line scan trajectory for the case of a) ideal selection field and b) non-ideal selection field, showing every fifth line. The targeted FOV was 4×4 cm^2 (marked with the dashed red square). In the non-ideal case, the trajectory warps in regions away from the scanner iso-center, extending outside the intended FOV. c) The direct x-space reconstructed image using the actual FFP trajectory closely matches the corrected image in Fig. 3.8c.

3.3.6 Demonstration on a Vasculature Phantom

To demonstrate both the manifestation of the non-ideal selection field induced artifacts and the effectiveness of the unwarping algorithm on a more complex case, imaging simulations were performed using the vasculature phantom shown in Fig. 3.10a. Here, the phantom was designed such that it extends beyond the targeted 4×4 cm ^{2} FOV. All simulation parameters were kept the same as before (see Section II.II). The images under ideal and non-ideal selection fields are displayed in Fig. 3.10b-c, respectively. In the reconstructed image, some of the branches of the vasculature phantom that are outside the targeted FOV are pushed into the image due to warping (see the red arrows in Fig. 3.10c). Next, the reconstructed image was unwarped using the displacement maps in Fig. 3.8a-b. As shown in the corrected image in Fig. 3.10d, the branches near the edges/corners of the FOV are successfully mapped back to their correct positions. For this more complex case, the resolution loss towards the edges of the FOV is not as noticeable as that in Fig. 3.8c.

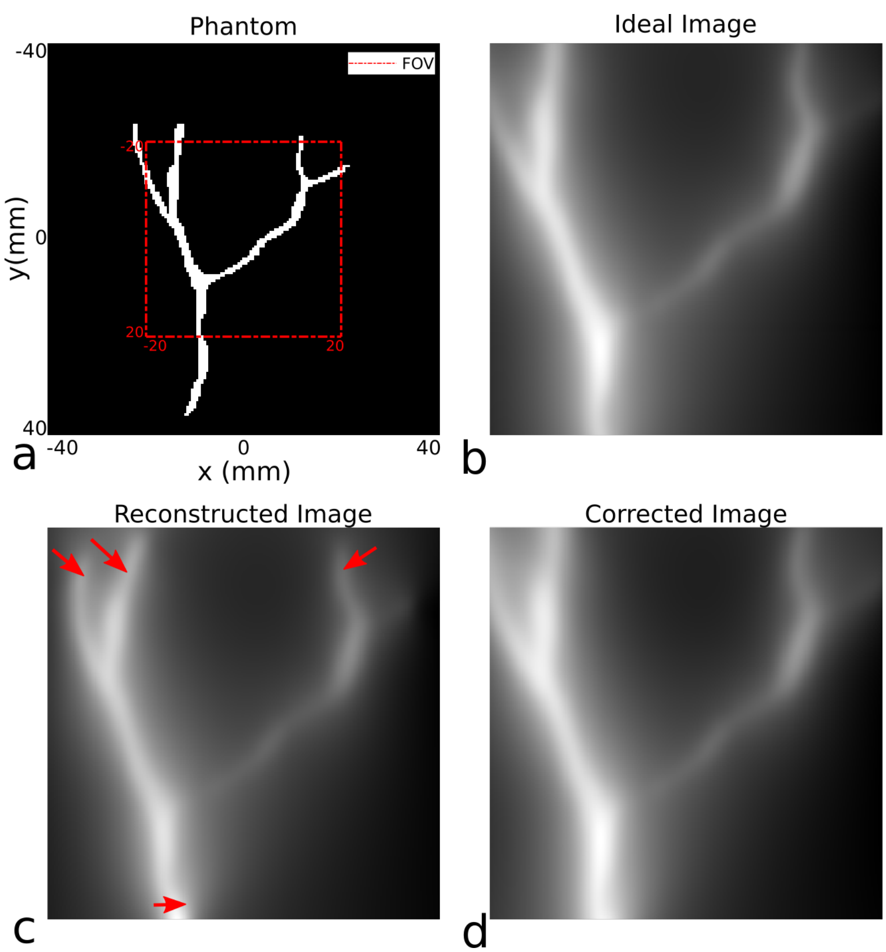

Figure 3.10: a) A vasculature phantom extending beyond the targeted 4×4 cm^2 FOV (dashed red box). b) Image for the ideal selection field, c) x-space reconstructed image for the non-ideal selection field, and d) corrected image after unwarping.

3.4 Discussion

The results in this thesis show that a geometric warping artifact occurs in x-space reconstructed images, if the targeted FOV extends beyond the linear region of the selection field. These artifact occur due to a combination of two factors: selection field non-linearity, combined with a focus field and drive field that ignores this non-ideality. Hence, instead of the unwarping method presented in this thesis, one can also adjust the focus field and drive field amplitudes to counteract the effects of the selection-field non-ideality. Note that while this would alleviate the warping problem, the resolution loss away from the center of the scanner would still be observed.

Alternatively, instead of using a focus field, one may move the phantom/subject along the bore of the scanner (i.e., in a sliding-table fashion) to remain in the linear region of the selection field. Such an approach was previously proposed for the purposes of enlarging the FOV, as an alternative to the focus field [35]. Accordingly, this solution would also alleviate the resolution loss issue. In a realistic setting, however, this technique can only fix the warping along the scanner bore direction.

In Fig. 3.4, the reconstructed image before unwarping displayed almost identical FWHM value as in the ideal case. The reason for this phenomenon is the fact that this analysis used FWHM to quantify the resolution. In addition to a resolution loss, the image is also experiencing warping, and these two effects counteract each other to yield almost identical PSF shape in the warped coordinate frame. If the analysis had instead used separability of two point sources as the resolution metric, the loss in resolution would be clear even in the warped image. While each point source would have the same FWHM in the warped image, they would be brought closer because of warping, making it harder and harder to separate them at positions away from the center of the scanner. In theory, using the separability metric for the quantification of resolution should yield identical results as the FWHM measured *after* unwarping.

If the selection field is known, one can compute the actual FFP trajectory and perform a direct x-space reconstruction, as shown in Fig. 3.9c. It should be mentioned that this approach is not practical, since the actual FFP trajectory would need to be recomputed every time a drive field parameter (i.e., frequency, amplitude, and/or trajectory type) is changed. Furthermore, because pFOVs lie on warped lines as shown in Fig. 3.9b, a pFOV-overlap-based DC recovery algorithm can become computationally more challenging. In contrast, the displacement map is independent of the trajectory, and the DC recovery algorithm is straightforward if one assumes a straight line. Hence, it is considerably more practical to perform x-space reconstruction by ignoring selection field non-ideality, and then correcting its effects via unwarping, as done in Fig. 3.8c.

A previous work proposed a hybrid solution where a system function approach was adapted to x-space images to counteract the warping effects [36]. Accordingly, the PSF (or its Fourier transform) measured at each pixel position was inserted into an image-based system matrix, which was then used during the image reconstruction step. Note that the system matrix in that case depends on not just the scanner setup, but also the nanoparticle characteristics. In contrast, the unwarping approach presented in this thesis solely depends on the selection field and is independent of the nanoparticle type.

The unwarping approach is expected to work successfully as long as the FOV does not extend too far outside the linear region and into the near-constant selection field region. If the selection field gradient falls down to zero, signals from different positions would be mapped to the same location in the reconstructed image. In such a case, an unwarping algorithm (or direct reconstruction) would fail to separate those signals. Hence, one needs to remain in a region where the selection field maintains a non-zero gradient. As seen in Fig. 3.8, the unwarped image reflects the positions of the point sources accurately, albeit with a resolution loss near the edges of the FOV. Hence, while warping effects can be corrected, resolution loss is inherent to how it scales with the gradient. Therefore, the size of the FOV may need to be chosen to maintain a target resolution.

This thesis incorporated the effects of selection-field-induced artifacts only.

Previous works considered the effects of transmit/receive coil non-idealities [27, 37]. It remains an important future work to investigate the effects of those additional non-idealities on x-space reconstruction, and to find the trade-off between hardware fidelity and image quality.

Chapter 4

Magnetic Particle Fingerprinting using Arbitrary Waveform Relaxometer

This chapter is based on the publication titled "Magnetic Particle Fingerprinting using Arbitrary Waveform Relaxometer", E. Yağız, M. Ütkür, C.B. Top, E. U. Sarıtaş. Proc of the 10th International Workshop on Magnetic Particle Imaging, Virtual Conference, September 2020.

4.1 Background

MPI offers promising capability for quantifying viscosity and temperature in the biologically relevant range, or distinguish different types of nanoparticles via the response of the nanoparticles used as contrast agents [38, 39]. As aforementioned in Section 2.4, the behavior of the nanoparticles are relatively complicated to model and to simulate, making the experimental work in this field even more valuable. In literature, there are several approaches to achieve a mapping from the signal response to the parameter of interest (e.g., viscosity/temperature) or simply to distinguish two different types of nanoparticles. One popular approach is to use the ratio of the harmonics in the acquired signal, since relaxation effectively changes the spectrum content of the nanoparticle signal [12, 38, 39]. Even though these studies already displayed the possibility of quantitative mapping in MPI, there is a non-negligible overhead of calibration per nanoparticle type and per any scanner parameter. Another method called TAURUS (see Section 2.4.1), which requires neither calibration nor a-priori information about the nanoparticles, has been presented recently [20, 14]. While TAURUS directly estimates the effective relaxation time from the nanoparticle signal, it still requires the knowledge of optimum drive field (DF) parameters for a given application type.

As the nanoparticle signal changes with DF parameters [18], one potential problem for quantitative mapping applications of MPI is the optimization of DF parameters, mainly the fundamental frequency f_0 (Hz) and the peak magnetic field amplitude B_{peak} (T). This problem remains persistent independent of the estimation pipeline and requires a solution for the hardware setup.

In this thesis, a characterization of nanoparticle response by a rapid coverage of the "*excitation space*" (i.e., the 2-D space constructed by DF parameters B_{peak} and f_0) is proposed. This technique is named as "*Magnetic Particle Fingerprinting*" (MPF), and the τ-*fingerprint* of the nanoparticle is mapped across a wide range of field strength/frequencies using an Arbitrary Waveform Relaxometer (AWR). Unlike standard MPI and magnetic particle spectrometer (MPS) systems that operate at a fixed frequency, an AWR that can operate at any frequency was recently proposed to enable rapid optimization of DF parameters [40].

With the proposed framework, this thesis shows that 150 (B_{peak}, f_0) pairs in the excitation space can be traversed in 0.5 seconds and the time response of the nanoparticles can be conveniently mapped to a single parameter τ, which can then be used as a fingerprint to distinguish different nanoparticles and/or local environmental properties such as viscosity and temperature.

4.2 Methods

4.2.1 Rapid Excitation Space Coverage

In this study, the excitation space is used to describe the space consisting of two main DF parameters: peak magnetic field amplitude B_{peak} (T) and fundamental frequency f_0 (Hz) (i.e., space formed by $B_{peak} \times f_0$).

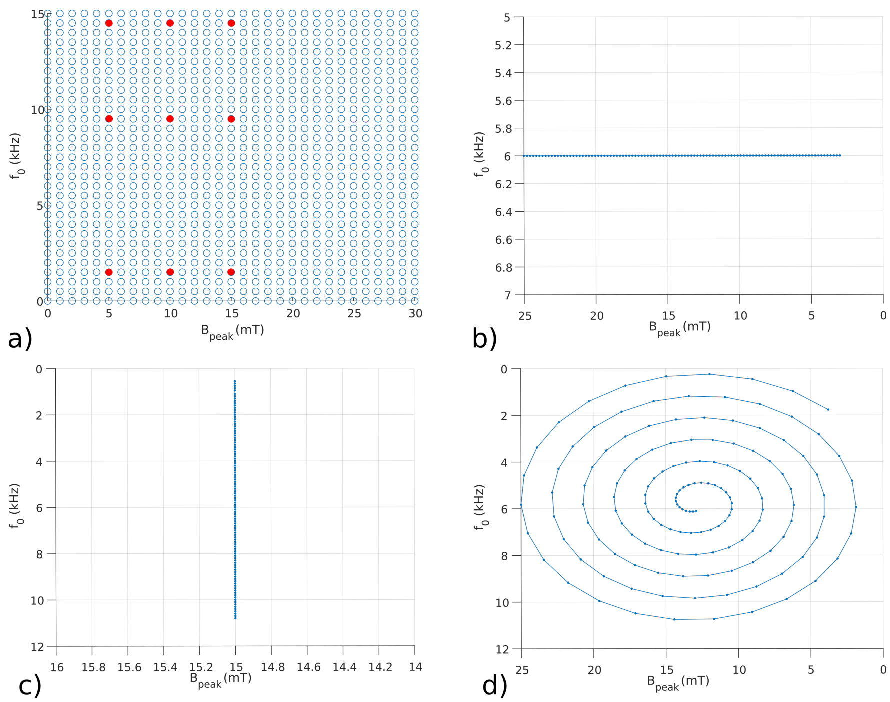

Figure 4.1: a) Excitation space consisting of $\left(B_{peak}, f_0\right)$ pairs. The red dots show that only a few frequencies can be used in typical quantitative MPI studies. b) An example linear trajectory in excitation space. Here, the frequency f_0 is kept constant and the B_{peak} values are traversed in the range of interest. c) Another example linear trajectory in excitation space. Here, the B_{peak} value is kept constant and the frequency is traversed in the range of interest. d) A spiral trajectory in excitation space. Note that, with this approach a wider range of $\left(B_{peak}, f_0\right)$ pairs are covered in a single experiment.

Previous techniques in the literature could only cover a small portion of the excitation space as depicted in Figure 4.1a, due to the need to separately tune the MPI or MPS system at each drive field frequency. Since the AWR setup does not require any tuning, it can support arbitrary waveforms. By alleviating the hardware limitations, virtually every (B_{peak}, f_0) pair can be used to excite the nanoparticles. Here, to achieve a rapid coverage of the excitation space, several different trajectories are proposed as shown in Figure 4.1b-d.

For the first set of experiments, the excitation space was traversed via two different trajectories: linear (line-by-line) (Figure 4.1b-c) and spiral trajectory (Figure 4.1d). After choosing the range of interest for B_{peak} and f_0, and the type of trajectory, the corresponding time-domain DF waveform was constructed as,

$$B_d(t) = \sum_{i=1}^{N} B_{peak,i} \sin\left(2\pi f_{0,i}(t - \Delta t_i)\right)\left(u\big(t - \Delta t_i\big) - u\big(t - \Delta t_i - \frac{N_{cycle}}{f_{0,i}})\right) \tag{4.1}$$

where $B_d(t)$ is the DF waveform, N is the number of excitation pairs to cover, $B_{peak,i}$ is the i^{th} peak magnetic field amplitude, $f_{0,i}$ is the i^{th} fundamental frequency, and Δt_i is the time shift to stack different sinusoids one after the other. Note that for each (B_{peak}, f_0) pair in the excitation space, N_{cycle} of sinusoidals with frequency $f_{0,i}$ and amplitude $B_{peak,i}$ were generated. In this study, $N_{cycle} = 10$ was used.

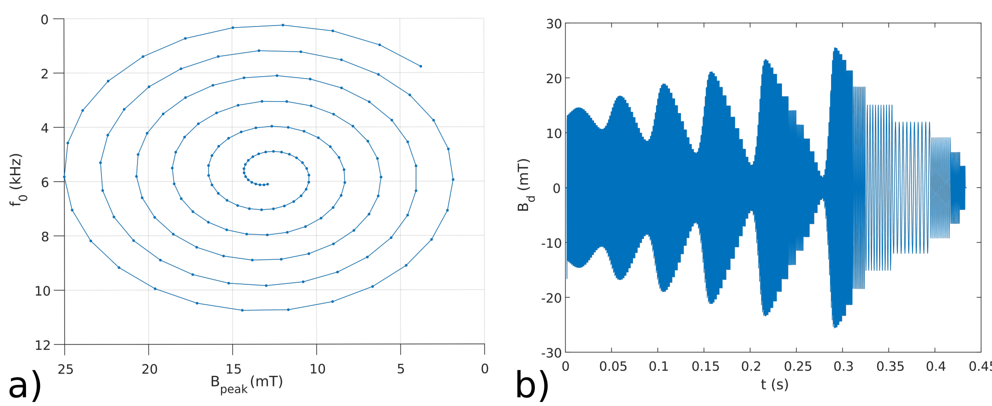

Figure 4.2: a) Spiral trajectory in excitation space. b) The DF waveform constructed using Equation 4.1 with 10 cycles for each sinusoid and $N = 150$. Note that 150 individual experiments are now compressed under 0.5 seconds.

Figure 4.2 shows an example spiral trajectory, together with the corresponding DF waveform. After the trajectory was chosen and the corresponding waveform was used to excite the nanoparticles, TAURUS technique was used to map τ at each $\left(B_{peak}, f_0\right)$ point on the trajectory. This way, it is possible to acquire information from over a 150 $\left(B_{peak}, f_0\right)$ pairs in under 0.5 seconds, thus combining many individual experiments at once in an accelerated fashion.

4.2.2 In-house Arbitrary Waveform Relaxometer Setup

Typical MPI scanners and MPS setups are built as resonant systems, i.e., a matching circuitry is required at each operating fundamental frequency. Therefore, the aforementioned mapping studies can only collect data at a few frequencies (f_0) and selected number of peak magnetic field amplitudes (B_{peak}). Recently, to avoid such hardware limitations, a new type of relaxometer called AWR was proposed [40]. The drive coil of an AWR setup is designed to have very low inductance, obviating the need for a matching circuit at a wide range of frequencies. This kind of freedom in hardware opens new possibilities in terms of imaging and spectrometer experiments, such as characterization of nanoparticles for viscosity/temperature mapping and optimization of DF parameters for specific applications.

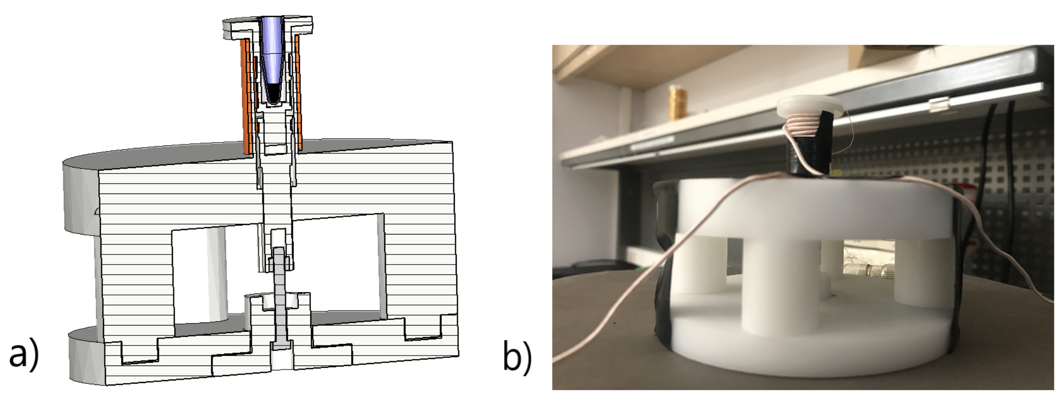

Figure 4.3: a) In-house AWR setup schematic. b) Actual photograph of the AWR setup.

For the experiments in this study an in-house AWR setup seen in Figure 4.3 was used [41]. This setup consists of a drive coil with 18 turns, with a relatively small 7 μH inductance that obviates impedance matching. The receive coil has a three-section gradiometer geometry, with 17, 20, and 5 turns. The shortest section can be adjusted manually via a knob to achieve 80 dB decoupling between drive/receive coils [41]. The bore is large enough to fit a 0.2 ml PCR tube.

4.2.3 Overall System

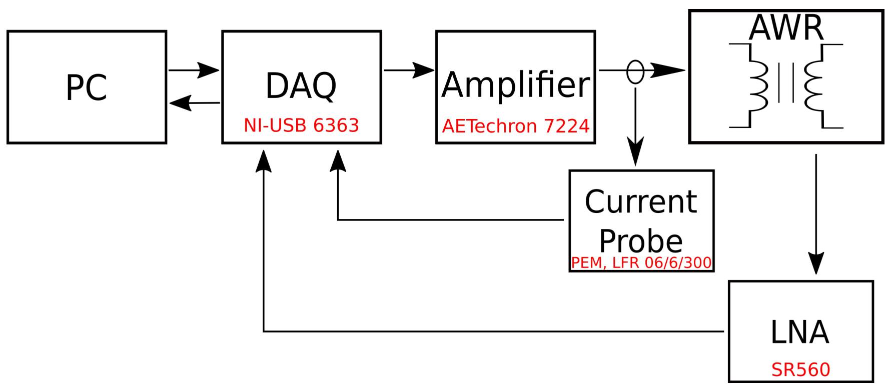

Figure 4.4: The schematic for the experimental setup also displaying the brand and model of the lab equipments.

The schematic for the overall experiment setup can be seen in Figure 4.4. Firstly, the DF parameters to traverse the excitation space were selected and the waveform was created in MATLAB as detailed in Section 4.2.1. After the time domain DF waveform was constructed, it was sent to a power amplifier (AETechron 7227) through a data acquisition card (NI-USB 6363) with 2 MS/s sampling rate. Since with the use of AWR there is no need for a matching circuitry, the amplifier was directly connected to the transmit coil of the AWR.

Before inserting the nanoparticles into the AWR setup, a manual calibration for the gradiometer was performed by rotating the knob that controls the relative position of the drive and receive coils. By tuning the gradiometer structure, firstly the direct-feedthrough (i.e., self-coupled DF signal) was minimized. Moreover, the non-linearities stemming from the amplifier or any coupled signal were reduced to the noise floor, so that the nanoparticle signal was not contaminated by other interfering sources.

Before each measurement took place, the magnetic field waveform was verified via a current probe (LFR 06/6/300, Power Electronic Measurements Ltd), that measured the current through the drive coil. A baseline measurement (i.e., signal with no nanoparticle in the AWR bore) was taken and recorded. Afterwards, the nanoparticle in 0.2 ml PCR tube was inserted into the AWR bore. The received signal was firstly amplified with a low-noise voltage pre-amplifier (SR560) and then fed to the same data acquisition card. The entire setup was controlled via MATLAB. In Figure 4.5, an example nanoparticle signal (Figure 4.5a) and the corresponding baseline signal (Fig. 4.5b) can be seen when the DF waveform in Figure 4.2b is applied.

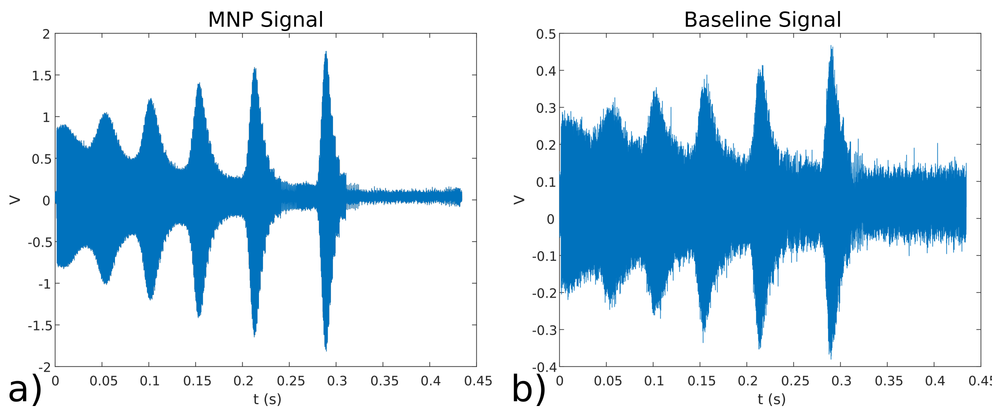

Figure 4.5: a) An example nanoparticle signal with respect to time. b) The corresponding baseline measurement. Note that each measurement was averaged by two times.

4.2.4 System Model in LTSpice

Since the key parameters in these experiments are $\left(B_{peak}, f_0\right)$, it is important to ensure that the magnetic field and the frequency that the nanoparticles are experiencing are the intended values so that true mapping can be obtained. For that goal, firstly the system was modeled in LTSpice using the system diagram shown in Figure 4.6a.

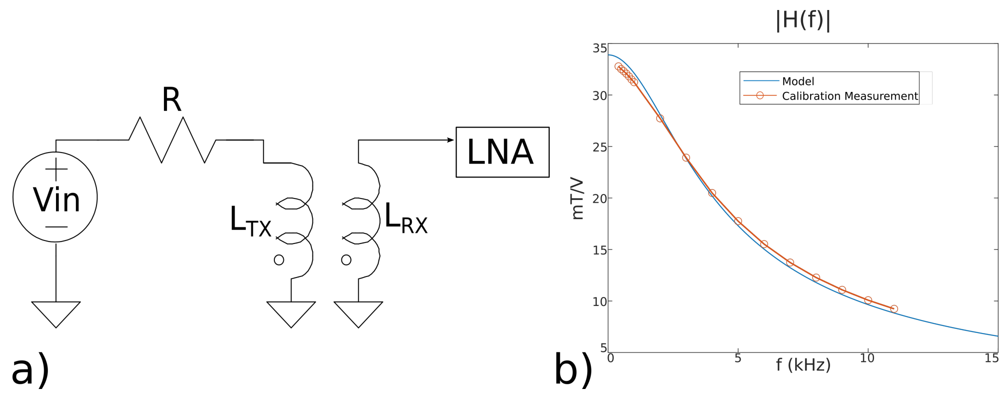

Figure 4.6: a) Simplified LTSpice model of the hardware setup. Here, V_{in} is the power amplifier and R is its equivalent series resistance. $L_{TX} = 7$ μH is the transmit side inductance of the AWR. Note that the model for the transmit side also includes a series resistance of 2 mΩ. $L_{RX} = 7$ μH is the receive side inductance of the AWR. The receive side is then connected to the LNA, hence terminated with high series impedance. b) The model estimate (blue) and the calibration measurement (red) for the transfer function $H(f) = B_{peak}(f)/V_{in}(f)$, taken using a Hall effect gaussmeter. With this fitted curve, it is possible to obtain desired magnetic field amplitude at a given frequency.

After setting up the model in LTSpice, the designed DF waveform in MATLAB is fed to the model and the current through the inductor L_{TX} is simulated. Since the setup (Figure 4.4) is controlled via a voltage amplifier, firstly transfer function $H(f) = B_{peak}(f)/V_{in}(f)$ (i.e., the magnetic field amplitude per applied voltage by the power amplifier) was calculated as a function of frequency. Then, experiments were performed to verify the simulation results. A MATLAB script was used to send a sinusoidal signal to the AWR setup with a given frequency in a range of frequencies of interest and then the magnetic field within the AWR bore was measured via a Hall effect gaussmeter (LakeShore 475 DSP Gaussmeter). If the magnetic field amplitude did not match the desired value, then minding the difference the amplitude of the sinusoidal signal was adjusted until the measured magnetic field showed at most 5% deviation from the desired magnetic field. The model estimate for the amplitude of the transfer function versus the fundamental frequency can be seen together with calibration measurements in Figure 4.6b showing very good agreement between the model and the measurements.

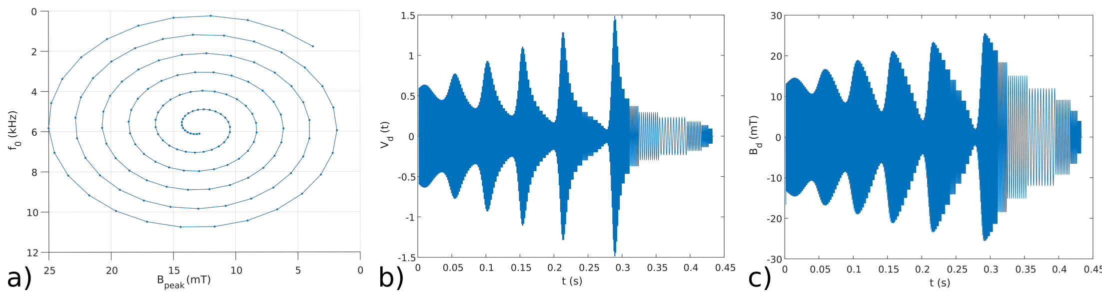

Figure 4.7: a) Spiral trajectory in excitation space. b) The voltage DF waveform constructed using Equation 4.2 where V_{in}'s are found through Fig. 4.6b with 10 cycles for each sinusoid and $N = 150$. c) The magnetic field corresponding to the voltage DF seen in (b).

The DF waveform $B_d(t)$ cannot directly be sent to the drive coil of the AWR. Instead, a voltage DF waveform is sent such that at each $f_{0,i}$ the desired $B_{peak,i}$ is achieved. The necessary amplitude V_{in} is found through the fitted curve for the transfer function shown in Figure 4.6b. Then, the applied voltage can be expressed as:

$$V_d(t) = \sum_{i=1}^{N} V_{in} \sin\left(2\pi f_{0,i}(t - \Delta t_i)\right)\left(u\big(t - \Delta t_i\big) - u\big(t - \Delta t_i - \frac{N_{cycle}}{f_{0,i}}\big)\right) \quad (4.2)$$

where $V_d(t)$ is the voltage DF waveform. An example spiral trajectory together with the voltage DF waveform and the corresponding magnetic field is shown in Figure 4.7.

4.2.5 Sample Preparation

A first set of samples was prepared to demonstrate the effects of viscosity on nanoparticle signal across the excitation space. Samples at two different viscosities (0.89 mPa.s and 5.04 mPa.s) were prepared [42], as listed in Table 4.1. Each sample contained 10 μL of Nanomag-MIP nanoparticles (Micromod GmbH, Germany) with 89 mmol Fe/L. Deionized (DI) water and glycerol were added at varying volumes to reach a total volume of 20 μL for each sample. All measurements were performed at room temperature.

Viscosity (mPa.s)	0.89	5.04
Glycerol	0	10
DI Water	10	0
Glycerol Volume (%)	0	50

Table 4.1: Prepared samples at 2 different viscosity levels

A second set of samples was prepared to demonstrate the differences in signals from different nanoparticles across the excitation space. Accordingly, samples were prepared using 4 different nanoparticles: Nanomag-MIP, Synomag-D, Perimag, and Vivotrax. Each sample contained 10 μL of nanoparticles and 10 μL of DI water, with initial concentrations of 89 mmol Fe/L for Nanomag-MIP, 178 mmol Fe/L for Synomag-D, 303 mmol Fe/L for Perimag, and 98.21 mmol Fe/L for Vivotrax.

4.2.6 Magnetic Particle Fingerprinting Experiments

To see the ability of the MPF framework, several experiments were designed.

1. Experiment 1: Using a single nanoparticle sample (Nanomag-MIP at 0.89 mPa.s), the excitation space was covered in different trajectories (line-by-line and spiral as given in Figure 4.1). This experiment aimed to see the consistency of the MPF framework and compare different trajectories in excitation space.

2. Experiment 2: Using a single type of nanoparticle (Nanomag-MIP) at two different viscosities (0.89 mPa.s and 5.04 mPa.s), the excitation space was covered with the spiral trajectory. This experiment aims to see the capability of the MPF framework to differentiate viscosity and determine the regions of the excitation space that are most suitable for viscosity mapping.

3. Experiment 3: Using 2 different types of nanoparticles (Nanomag-MIP and Perimag) at the same viscosity level of 0.89 mPa.s, the excitation space was covered with the spiral trajectory. Here, it is known that these two nanoparticles are quite similar in terms of their physical properties [43, 44]. With this experiment, the aim is to see the consistency of the MPF framework.

4. Experiment 4: Using 3 different types of nanoparticles (Perimag, Vivotrax, and Synomag) at 0.89 mPa.s viscosity, the excitation space was covered with the spiral trajectory. With this, the aim is to see the capability of the MPF framework to differentiate different nanoparticles and to determine the regions in excitation space where the τ-fingerprints of the nanoparticles are similar or different.

4.3 Results

Here, the results for the system model of the AWR setup is given followed by the results of the τ-fingerprints corresponding to the MPF experiments outlined in Section 4.2.6.

4.3.1 Excitation Space Coverage

The construction for the DF waveform was outlined in Section 4.2.1. Here, the results for the system model are given together with the experimental verification. In addition, the excitation space trajectories are compared.

In Figure 4.8, the magnetic field estimate by the model is given for the spiral trajectory together with the actual magnetic field measurement. Here, note that the current on the drive coil was measured using a current probe, which was then converted to a magnetic field plot. It can be seen that even though the DF waveform seems to change abruptly from time to time, there is no unexpected distortions in the magnetic field plot. Importantly, the measured and modeled magnetic field plots show excellent agreement. Hence, the spiral trajectory is suitable to use in MPF experiments.

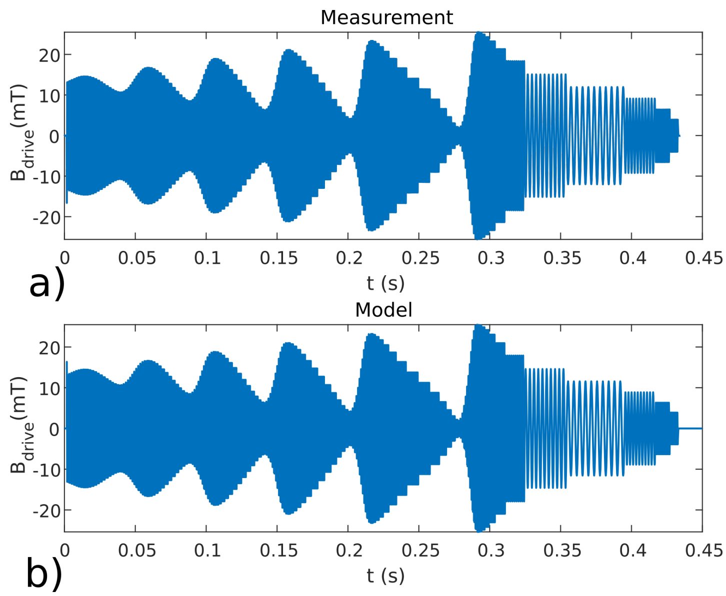

Figure 4.8: a) The drive field $B_d(t)$ corresponding to the spiral trajectory in excitation space. Here, note that the measurement took place via a current probe, then the magnetic field was found. b) LTSpice model estimate for the drive field $B_d(t)$. Here, the current through the inductor L_{TX} (Figure 4.6a) was simulated, then the magnetic field is calculated. Note that, the measurement and the model estimate agree quite well.

Similarly, the plots for the linear trajectories can be found in Figure 4.9 and 4.10. The trajectory in Figure 4.9 corresponds to the case where f_0 is kept constant and B_{peak} is increased, and Figure 4.10 corresponds to the case where B_{peak} is kept costant and f_0 is increased. Here, the experimental measurements can be seen in Figure 4.9a and 4.10a and the magnetic field plots of model estimates can be seen in Figure 4.9b and 4.10b. An important observation here is that, as shown in Figure 4.11a and Figure 4.11b, the product $B_{peak} \times f_0$ for the linear trajectories increases as the excitation space is traversed. As a result, the drive coil and/or the power amplifier may heat up. Hence, there is a slight drop in the magnetic field amplitude towards the middle of the plot as seen in in Figure 4.10a.

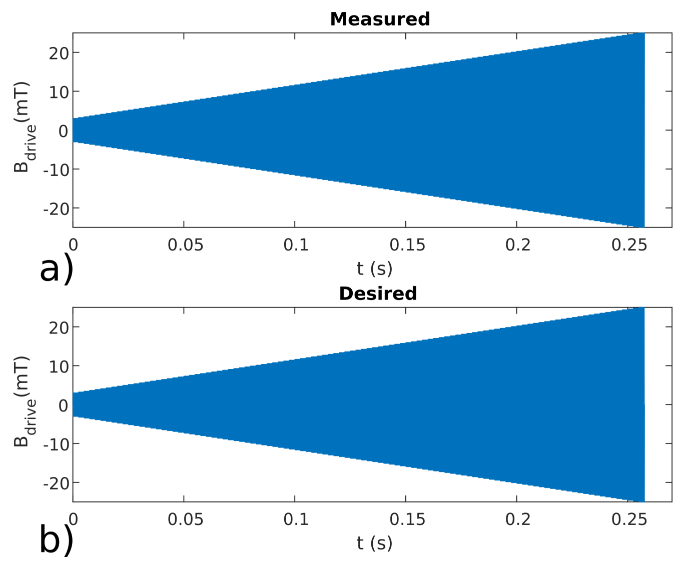

Figure 4.9: a) The drive field $B_d(t)$ (s) corresponding to the linear trajectory in excitation space (constant f_0). Same procedure was applied as in Figure 4.8. b) LTSpice model estimate for the drive field $B_d(t)$. Note that, the measurement and the model estimate agree quite well.

In comparison, Figure 4.11c displays $B_{peak} \times f_0$ product for the spiral trajectory. As seen in this plot, traversing the excitation space in a spiral fashion creates a duty cycle effect, so that the coil does not heat up as in the case of linear trajectories. Hence, the spiral trajectory is more suitable for the experiments, since it rapidly covers a wider range of parameters while enabling repeatable experiments without overheating the setup.

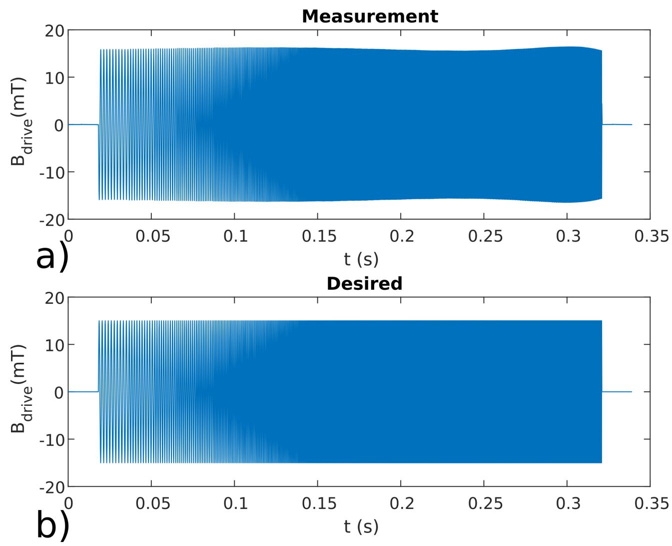

Figure 4.10: a) The drive field $B_d(t)$ (s) corresponding to the linear trajectory in excitation space (constant B_{peak}). Same procedure was applied as in Figure 4.8. b) LTSpice model estimate for the drive field $B_d(t)$. Note that, the measurement and the model estimate agree quite well.

4.3.2 Magnetic Particle Fingerprinting Experiments

1. Experiment 1 results for τ-fingerprints of a single nanoparticle type for different trajectories are shown in Figure 4.12 as 3-D plots. In Figure 4.12a, the results are given in terms of the relaxation time constant τ (μs). In Figure 4.12b, the time constants are normalized by the period at f_0 (i.e., by $T_0 = 1/f_0$). These results demonstrate the consistency of the MPF framework, as the different trajectories show excellent agreement in the estimated τ values in regions where they overlap. Even though the results are consistent, the spiral trajectory was preferred in the remaining experiment since its coverage is wider and experiments are repeatable (as explained in Section 4.3.1).

2. Experiment 2 results for τ-fingerprints of a single type of nanoparticle at two different viscosity levels are shown in Figure 4.13. In this experiment, the excitation space was covered using the spiral trajectory. Again, in Figure 4.13a the results are given for the τ-fingerprint and in Figure 4.13b the

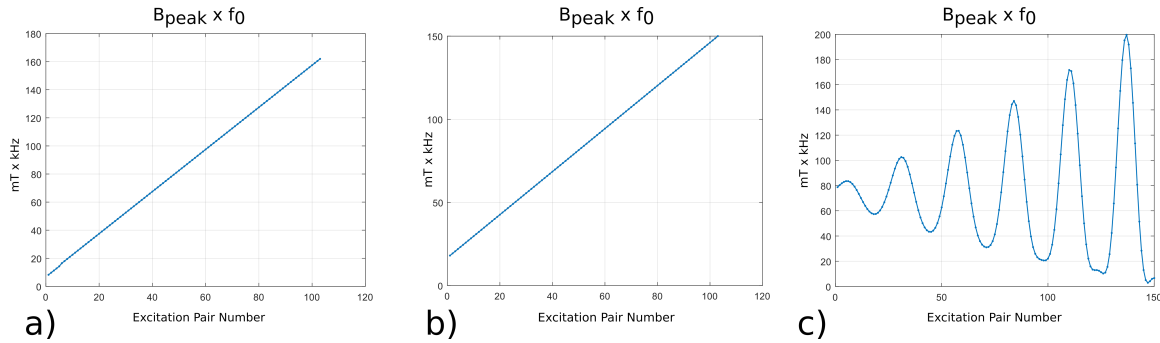

Figure 4.11: The product of $B_{peak} \times f_0$ corresponding to a) the linear trajectory in which B_{peak} is kept constant, b) the linear trajectory in which f_0 is kept constant, and c) the spiral trajectory. Note that the product oscillates in (c), creating a duty cycle effect and preventing the coil from heating up, whereas in (a) and (b) the product increases throughout the trajectory.

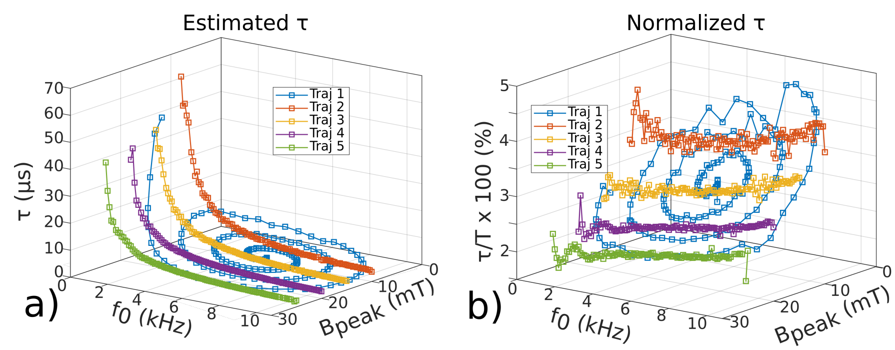

Figure 4.12: a) 3-D plot of the τ-fingerprint for the Nanomag-MIP at 0.89 mPa.s for different trajectories. b) 3-D plot of the normalized τ-fingerprint. The normalization is done with the respective periods.

results are given for the normalized τ. It should be noted that these two samples can be distinguished easily when the applied magnetic field peak value B_{peak} decreases and/or the frequency f_0 decreases. These results demonstrate the viscosity mapping potential of MPF.

3. Experiment 3 results comparing τ-fingerprints of Nanomag-MIP and Perimag nanoparticles are displayed in Figure 4.14. In this experiment, again the excitation space was covered in a spiral fashion. In Figure 4.14a the results are shown for the τ-fingerprints and in Figure 4.14b the results are shown for the normalized τ-fingerprints. Additionally, for this experiment

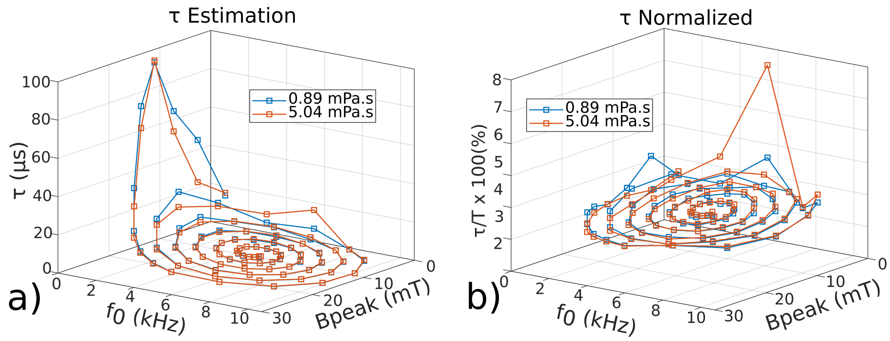

Figure 4.13: a) 3-D plot for the τ-fingerprints for the Nanomag-MIP at 0.89 mPa.s (blue) and at 5.04 mPa.s (red). b) 3-D plot for the normalized τ-fingerprints. Here note that in both plots the responses are quite similar, and the ability to distinguish increases when the peak magnetic field B_{peak} decreases and/or the frequency f_0 decreases.

4^{th} order median filtering was applied for τ values along the trajectory. It can be seen that, the response of these two nanoparticles are quite similar throughout the excitation space, which was an expected result since the specifications for Nanomag-MIP and Perimag are quite similar.

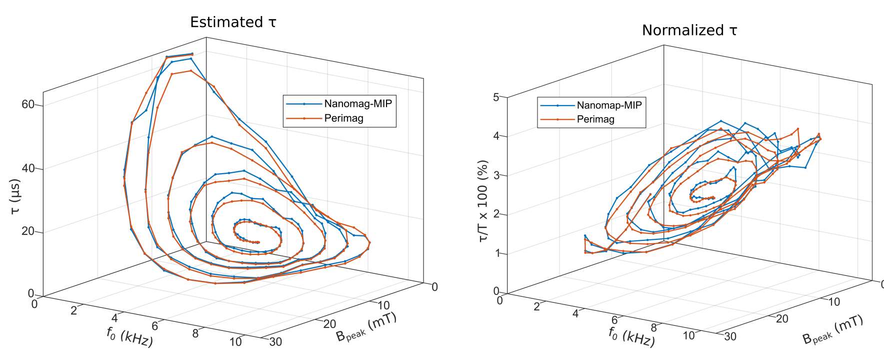

Figure 4.14: a) 3-D τ-fingerprint plot for the Nanomag-MIP (blue) and Perimag (red). Both samples were at 0.89 mPa.s viscosity. b) 3-D plot for the normalized τ curves of the Nanomag-MIP (blue) and the Perimag (red) samples. Note that for better visualization, 4^{th} order median filtering was applied on the curves.

4. Experiment 4 results comparing τ-fingerprints of 3 different types of nanoparticles are shown in Figure 4.15. For this experiment two figures are added with different perspectives so that it is easier to see the individual curves of the nanoparticles. Again, the excitation space was covered in a spiral fashion and a 4^{th} order median filter was applied. Here note that, the τ-fingerprints of the nanoparticles Synomag, Vivotrax, and Perimag can be visually distinguished from one another, thus enabling the differentiation of nanoparticles.

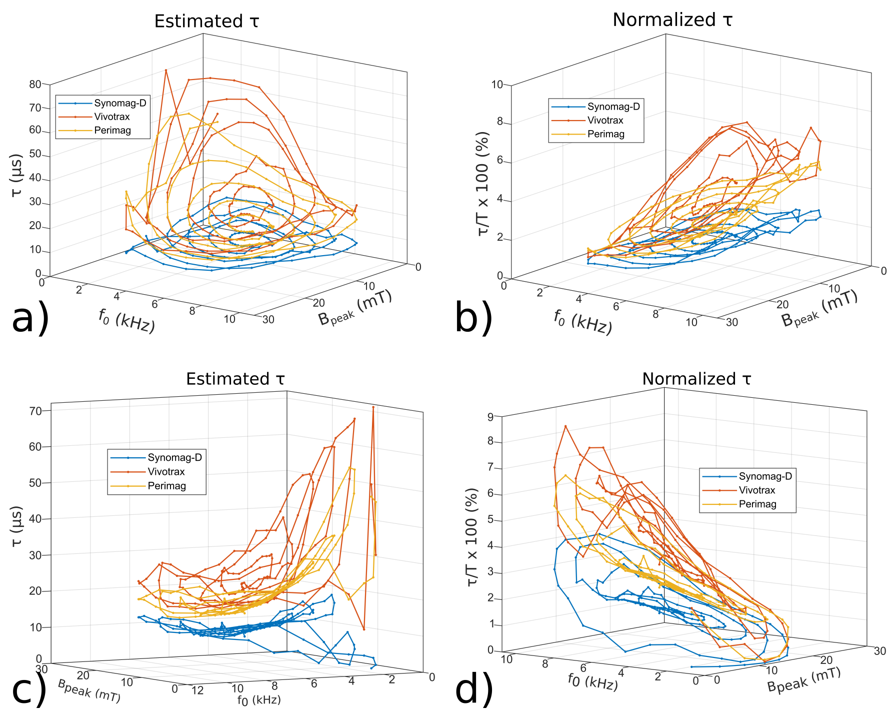

Figure 4.15: a) 3-D τ-fingerprint plot for the Synomag-D (blue), Vivotrax (red), and Perimag (yellow). All samples were at 0.89 mPa.s viscosity level. b) 3-D plot for the normalized τ. c) The 3-D plot seen in (a) is rotated for better visual separation of τ-fingerprints of the nanoparticles. d) Rotated version of the normalized τ-fingerprint seen in (b). Note that for better visualization 4^{th} order median filtering was applied.

After demonstrating the ability of the MPF framework to distinguish different nanoparticles, a significance test was applied also on the normalized τ-fingerprints with the default threshold value of $p = 0.05$. The results of this significance test can be seen in Figure 4.16. As a verification for the visual inspection, (Figure

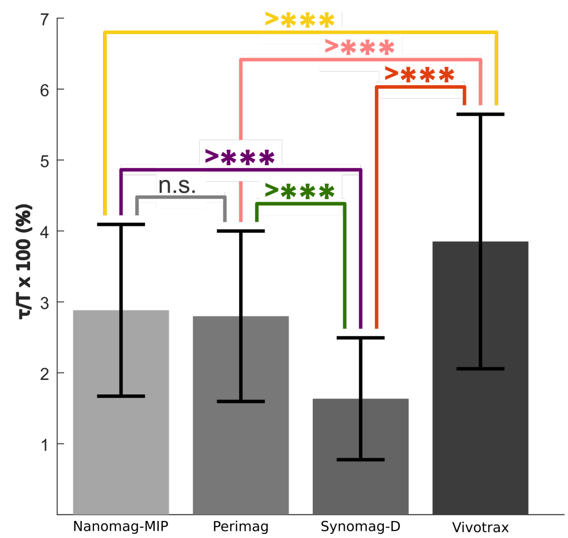

Figure 4.16: Significance test results presented as a bar chart. It can be seen that the pairs Nanomag-MIP - Vivotrax, Nanomag-MIP - Synomag and Vivotrax - Synomag are significantly different. As shown in Figure 4.14 the response of Nanomag-MIP and Perimag are found to be similar to each other.

4.15), the overall τ-fingerprints of the nanoparticles Nanomag-MIP, Synomag-D, and Vivotrax are significantly different from each other. Similarly, Synomag-D and Vivotrax are found to be significantly different from each other. As expected based on the results in Figure 4.14, the τ-fingerprints of Nanomag-MIP and Perimag cannot be separated from each other since there is no significant difference.

4.4 Discussion

The results given in this chapter indicate that different viscosities, different nanoparticles can be distinguished using the proposed MPF technique. One can expect to see unique trends at different temperatures, as well, enabling simultaneous mapping of viscosity and temperature with the proposed technique.

Even though the obtained results are MPF experiments laid out in this chapter are promising to achieve a powerful tool in quantitative MPI, there are several issues that need to be addressed in more detail. Firstly, the results should be verified and the error margins should be determined by extensive experimental work. More importantly, there are experiments in the field stating that the response of the nanoparticles also change in the presence of a static magnetic field such as the selection field of an MPI scanner. Therefore, for this method to be translated to quantitative imaging scenarios, similar experiments should be conducted and the τ-fingerprints should be recorded into a dictionary under the presence of a selection field.

In this work, the range covered in excitation space was selected such that it includes the frequencies and peak magnetic field amplitudes popularly used in MPI/MPS studies. However, as seen in the results, the ability to distinguish different types of nanoparticles and/or viscosities is more prominent in certain parts of the excitation space. Hence, a tailored trajectory can be chosen the application of interest such that the regions in which the nanoparticle responses differ are covered in a finer interval.

Chapter 5

Conclusions

In conclusion, in this thesis firstly the non-ideal selection-field-induced artifacts in x-space MPI are demonstrated via both theoretical derivations and imaging simulations. It is shown that the image warping can take place when the FOV is enlarged, such that the gradient of the selection field is no longer constant. This situation arises if the system is not specifically designed for high fidelity linearity in a large volume. The resulting distortion, however, is relatively benign and a corrected image can be obtained using image unwarping algorithms. The resolution loss, on the other hand, remains in the unwarped image and may be the determining factor for the size of the FOV. As MPI is being developed for clinical usage, such practical problems are needed to be investigated so that the hardware design considerations and the trade-offs between design parameters are better understood.

Additionally, in this thesis, an accelerated framework called Magnetic Particle Fingerprinting (MPF) is proposed to rapidly cover the excitation space and characterize the unique τ-fingerprint of a nanoparticle under different environmental settings. This technique has a variety of potential applications, including rapid and simultaneous quantification of several parameters (e.g., viscosity, temperature, nanoparticle type, etc.). Moreover, it can be used to determine the optimum DF parameters for a given mapping application.

Bibliography

[1] B. Gleich and J. Weizenecker. Tomographic imaging using the nonlinear response of magnetic particles. *Nature*, 435(7046):1214–1217, 2005. doi: 10.1038/nature03808.

[2] J. Weizenecker, J. Borgert, and B. Gleich. A simulation study on the resolution and sensitivity of mangnetic particle imaging. *Physics in Medicine & Biology*, 52(21):6363–74, 2007. doi: 10.1088/0031-9155/52/21/001.

[3] Emine U. Saritas, Patrick W. Goodwill, Laura R. Croft, Justin J. Konkle, Kuan Lu, and Steven M. Conolly. Magnetic particle imaging (mpi) for nmr and mri researchers. *Journal of Magnetic Resonance*, 229:116–126, 2013. doi: 10.1016/j.jmr.2012.11.029.

[4] J. Weizenecker, B. Gleich, J. Rahmer, H. Dahnke, and J. Borgert. Three-dimensional real-time in vivo magnetic particle imaging. *Physics in Medicine & Biology*, 54(5), 2009. doi: doi.org/10.1088/0031-9155/54/5/L01.

[5] K. Lu, P. W. Goodwill, E. U. Saritas, B. Zheng, and S. M. Conolly. Linearity and shift invariance for quantitative magnetic particle imaging. *IEEE Transactions on Medical Imaging*, 32(9):1565–1575, 2013. doi: 10.1109/tmi.2013.2257177.

[6] Elaine Y. Yu, Mindy Bishop, Bo Zheng, R. Matthew Ferguson, Amit P. Khandhar, Scott J. Kemp, Kannan M. Krishnan, Patrick W. Goodwill, and Steven M. Conolly. Magnetic particle imaging: A novel in vivo imaging platform for cancer detection. *Nano Lett.*, 17:1648–1654, 2017. doi: 10.1021/acs.nanolett.6b04865.

[7] Bo Zheng, Tandis Vazin, Patrick W. Goodwill, Anthony Conway, Aradhana Verma, Emine Ulku Saritas, David Schaffer, and Steven M. Conolly. Magnetic particle imaging tracks the long-term fate of in vivo neural cell implants with high image contrast. *Scientific Reports*, 2015. doi: 10.1038/srep14055.

[8] Bo Zheng, Marc P. von See, Elaine Yu, Beliz Gunel, Kuan Lu, Tandis Vazin, David V. Schaffer, Patrick W. Goodwill, and Steven M. Conolly and. Quantitative magnetic particle imaging monitors the transplantation, biodistribution, and clearance of stem cells in vivo. *Theranostics*, 6:291–301., 2016. doi: 10.7150/thno.13728.

[9] Kolja Them, J Salamon, P Szwargulski, S Sequeira, M G Kaul, C Lange, H Ittrich, and Tobias Knopp. Increasing the sensitivity for stem cell monitoring in system-function based magnetic particle imaging. *Physics in Medicine & Biology*, 61:3279–3290, 2016. doi: doi:10.1088/0031-9155/61/9/3279.

[10] J. Rahmer, J. Weizenecker, B. Gleich, and J. Borgert. Signal encoding in magnetic particle imaging: properties of the system function. *BMC Medical Imaging*, 9(4):485–491, 2009. doi: 10.1186/1471-2342-9-4.

[11] P. W. Goodwill and S. M. Conolly. The X-Space Formulation of the Magnetic Particle Imaging Process: 1-D Signal, Resolution, Bandwidth, SNR, SAR, and Magnetostimulation. *IEEE Transactions on Medical Imaging*, 29(11): 1851–1859, 2010. doi: 10.1109/tmi.2010.2052284.

[12] R. Matthew Ferguson, Amit P Khandhar, Christian Jonasson, Jakob Blomgren, Christer Johansson, and Krishnan. Size dependent relaxation properties of monodisperse magnetite nanoparticles measured over seven decades of frequency by ac susceptometry. *IEEE Transactions on Magnetics*, 49(7): 3441–3444, 2013. doi: 10.1109/TMAG.2013.2239621.

[13] Robert J. Deissler, Yong Wu, and Michael A. Martens. Dependence of brownian and neel relaxation times on magnetic field strength. *Medical Physics*, 41(1):012301, 2014. doi: 10.1118/1.4837216.

[14] Mustafa Utkur, Yavuz Muslu, and Emine Ulku Saritas. Relaxation-based

color magnetic particle imaging for viscosity mapping. *Applied Physics Letters*, 115(15):152403, 2019. doi: 10.1063/1.5110475.

[15] Gösta Tibblin M.D., S.-E.Bergentz M.D, J.Bjure M.D., and L.Wilhelmsen M.D. Hematocrit, plasma protein, plasma volume, and viscosity in early hypertensive disease. *American Heart Journal*, 72:165–176, 1966. doi: 10.1016/0002-8703(66)90440-6.

[16] H Tohgi, H Yamanouchi, M Murakami, and M Kameyama. Importance of the hematocrit as a risk factor in cerebral infarction. *Stroke*, 9:369–374, 1978. doi: 10.1161/01.str.9.4.369.

[17] P. W. Goodwill and S. M. Conolly. Multidimensional x-space magnetic particle imaging. *IEEE Transactions on Medical Imaging*, 30(9):1581–1590, 2011. doi: 10.1109/TMI.2011.2125982.

[18] Jürgen Weizenecker, Bernhard Gleich, Jürgen Rahmer, and Jörn Borgert. Micro-magnetic simulation study on the magnetic particle imaging performance of anisotropic mono-domain particles. *Physics in medicine & biology*, 57(22):731727, 2012. doi: 10.1088/0031-9155/57/22/7317.

[19] L. R. Croft, P. W. Goodwill, and S. M. Conolly. Relaxation in x-space magnetic particle imaging. ieee transactions on medical imaging. *IEEE Transactions on Magnetics*, 31(12):2335–2342, 2012. doi: 10.1109/TMI.2012.2217979.

[20] Yavuz Muslu, Mustafa Utkur, Omer Burak Demirel, and Emine Ulku Saritas. Calibration-free relaxation-based multi-color magnetic particle imaging. *IEEE transactions on medical imaging*, 37(8):1920–1931, 2018. doi: 10.1109/tmi.2018.2818261.

[21] Y. Muslu, M. Utkur, O. B. Demirel, and E. U. Saritas. Calibration-free relaxation-based multi-color magnetic particle imaging. *IEEE Transactions on Medical Imaging*, 37(8):1920–1931, 2018. doi: 10.1109/TMI.2018.2818261.

[22] P. Vogel, M. A. Rückert, P. Klauer, W. H. Kullmann, P. M. Jakob, and V. C. Behr. Traveling wave magnetic particle imaging. *IEEE Transactions on Medical Imaging*, 33(2):400–407, 2014. doi: 10.1109/TMI.2013.2285472.

[23] F. Roméo and D. I. Hoult. Magnet field profiling: Analysis and correcting coil design. *Magnetic Resonance in Medicine*, 1(1):44–65, 1984. doi: 10.1002/mrm.1910010107.

[24] A. Weber, F. Werner, J. Weizenecker, T. Buzug, and T. Knopp. Artifact free reconstruction with the system matrix approach by overscanning the field-free-point trajectory in magnetic particle imaging. *Physics in Medicine and Biology*, 61(2):475–487, 2015. doi: 10.1088/0031-9155/61/2/475.

[25] J. Kybic, P. Thevenaz, A. Nirkko, and M. Unser. Unwarping of unidirectionally distorted EPI images. *IEEE Transactions on Medical Imaging*, 19 (2):80–93, 2000. doi: 10.1109/42.836368.

[26] S. J. Doran, L. Charles-Edwards, S. A. Reinsberg, and M. O. Leach. A complete distortion correction for MR images: I. Gradient warp correction. *Physics in Medicine and Biology*, 50(7):1343–1361, 2005. doi: 10.1088/0031-9155/50/7/001.

[27] H. Medimagh, P. Weissert, G. Bringout, K. Bente, M. Weber, K. Grafe, A. Cordes, and T. M. Buzug. Artifacts in field free line magnetic particle imaging in the presence of inhomogeneous and nonlinear magnetic fields. *Current Directions in Biomedical Engineering*, 1(1):245–248, 2015. doi: 10.1515/CDBME-2015-0061.

[28] M. Utkur, Y. Muslu, and E. U. Saritas. A 4.8 T/m Magnetic Particle Imaging Scanner Design and Construction. In *Proc. BIYOMUT 2017*, 2017. doi: 10.1109/BIYOMUT.2017.8479214.

[29] E. Bozkurt and E. U. Saritas. Signal-to-noise ratio optimized image reconstruction technique for magnetic particle imaging. *Journal of the Faculty of Engineering and Architecture of Gazi University*, 32(3):999–1013, 2017. doi: 10.17341/gazimmfd.337864.

[30] R. M. Ferguson, A. P. Khandhar, S. J. Kemp, H. Arami, E. U. Saritas, L. R. Croft, J. Konkle, P. W. Goodwill, A. Halkola, J. Rahmer, J. Borgert, S. M. Conolly, and K. M. Krishnan. Magnetic particle imaging with tailored iron oxide nanoparticle tracers. *IEEE Transactions on Medical Imaging*, 34(5): 1077–1084, 2015. doi: 10.1109/TMI.2014.2375065.

[31] T. Knopp and T. M. Buzug. *Magnetic Particle Imaging: An Introduction to Imaging Principles and Scanner Instrumentation*. Springer, Berlin/Heidelberg, 2012.

[32] S. I. Babic and C. Akyel. Improvement in the analytical calculation of the magnetic field produced by permanent magnet rings. *Progress In Electromagnetics Research C*, 5:71–82, 2008.

[33] P. W. Goodwill, J. J. Konkle, B. Zheng, E. U. Saritas, and S. M. Conolly. Projection x-space magnetic particle imaging. *IEEE Transactions on Medical Imaging*, 31(5):1076–1085, 2012. doi: 10.1109/TMI.2012.2185247.

[34] A. A. Ozaslan, A. Alacaoglu, O. B. Demirel, T. Çukur, and E. U. Saritas. Fully automated gridding reconstruction for non-Cartesian x-space magnetic particle imaging. *Physics in Medicine & Biology*, 64(16):165018, 2019. doi: 10.1088/1361-6560/ab3525.

[35] P. Szwargulski, N. Gdaniec, M. Graeser, M. Möddel, F. Griese, K. M. Krishnan, T. M. Buzug, and T. Knopp. Moving table magnetic particle imaging: A stepwise approach preserving high spatio-temporal resolution. *Journal of Medical Imaging*, 5(4):1, 2018. doi: 10.1117/1.JMI.5.4.046002.

[36] P. Vogel, T. Kampf, M. A. Ruckert, and V. C. Behr. Flexible and dynamic patch reconstruction for traveling wave magnetic particle imaging. *International Journal on Magnetic Particle Imaging*, 2(2), 2016. doi: 10.18416/ijmpi.2016.1611001.

[37] K. Murase, N. Banura, A. Mimura, and K. Nishimoto. Simple and practical method for correcting the inhomogeneous sensitivity of a receiving coil in magnetic particle imaging. *Japanese Journal of Applied Physics*, 54(3): 038001, 2015. doi: 10.7567/jjap.54.038001.

[38] Adam M. Rauwerdink and John B. Weaver. Viscous effects on nanoparticle magnetization harmonics. *Journal of Magnetism and Magnetic Materials*, 322(6):609–613, 2010. doi: 10.1016/j.jmmm.2009.10.024.

[39] Martin Möddel, Christian Meins, Jan Dieckhoff, and Tobias Knopp. Viscosity quantification using multi-contrast magnetic particle imaging. *New Journal of Physics*, 20(8):083001, 2018. doi: 10.1088/1367-2630/aad44b.

[40] Zhi Wei Tay, Patrick W Goodwill, Daniel W Hensley, Laura A Taylor, Bo Zheng, and Steven M Conolly. A high-throughput, arbitrary-waveform, mpi spectrometer and relaxometer for comprehensive magnetic particle optimization and characterization. *Scientific Reports*, 6(1):34180, 2016. doi: 10.1038/srep34180.

[41] Can Baris Top. An arbitrary waveform magnetic particle relaxometer with an asymmetrical three-section gradiometric receive coil. *Turkish journal of electrical engineering and computer sciences*, 28(3):1344–1354, 2020. doi: 10.3906/elk-1907-201.

[42] M. Sheely. Glycerol viscosity tables. *Industrial & Engineering Chemistry*, 24(9):1060–1064, 1932. doi: 10.1021/ie50273a022.

[43] Bo Zheng, Marc P. von See, Elaine Yu, Beliz Gunel, Kuan Lu, Tandis Vazin, David V. Schaffer, Patrick W. Goodwill, and Steven M. Conolly. Quantitative magnetic particle imaging monitors the transplantation, biodistribution, and clearance of stem cells in vivo. *Theranostics*, 6(3):291–301, 2016. doi: 10.7150/thno.13728.

[44] Justin J. Konkle, Patrick W. Goodwill, Daniel W. Hensley, Ryan D. Orendorff, Michael Lustig, and Steven M. Conolly. A convex formulation for magnetic particle imaging x-space reconstruction. *PLOS ONE*, pages 291–301, 2015. doi: 10.1371/journal.pone.0140137.